Cell Reports
Physical Science

Article

A structural bioplastic metafilm for durable passive radiative cooling

Graphical abstract

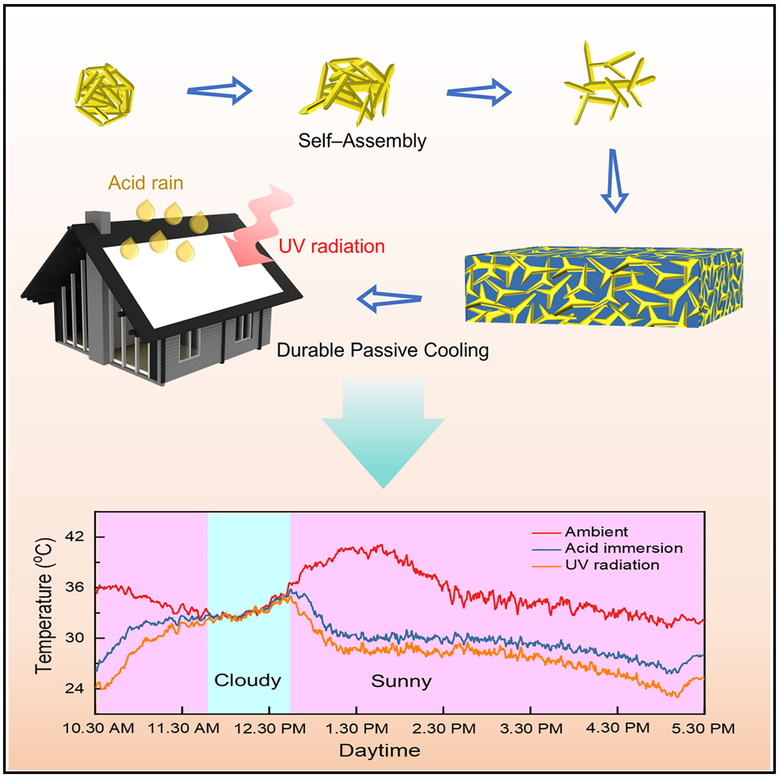

Highlights

- Enhanced optical properties while fully preserving the metafilm's complete degradability
- Tuned crystallization and pore formation to reveal self-assembly of the microstructure
- Achieved low thermal conductivity of 0.049 W m^{-1} K^{-1} and up to 9.2°C cooling under daytime
- Maintained 5°C–6.5°C cooling after acid exposure and 8-month-equivalent aging

Authors

Yangzhe Hou, Yamin Pan, Xianhu Liu, Jun Ma, Chuntai Liu, Changyu Shen

Correspondence

xianhu.liu@zzu.edu.cn

In brief

Hou et al. developed an advanced phase separation strategy to manufacture structural bioplastic metafilm featuring high-quality crystallinity and bi-continuous microstructures, enabling sustainable and durable outdoor passive radiative cooling with significant energy-saving potential.

Hou et al., 2025, Cell Reports Physical Science *6*, 102664
July 16, 2025
https://doi.org/10.1016/j.xcrp.2025.102664

CellPress

Please cite this article in press as: Hou et al., A structural bioplastic metafilm for durable passive radiative cooling, Cell Reports Physical Science (2025), https://doi.org/10.1016/j.xcrp.2025.102664

Cell Reports
Physical Science

CellPress
OPEN ACCESS

Article

A structural bioplastic metafilm for durable passive radiative cooling

Yangzhe Hou,[1,2,4] Yamin Pan,[1,2,4] Xianhu Liu,[1,2,3,5,*] Jun Ma,[2] Chuntai Liu,[1,3] and Changyu Shen[1,3]
[1]College of Materials Science and Engineering, National Engineering Research Center for Advanced Polymer Processing Technology, Zhengzhou University, Zhengzhou 450005, China
[2]UniSA STEM and Future Industries Institute, University of South Australia, Adelaide, SA 5095, Australia
[3]State Key Laboratory of Structural Analysis, Optimization and CAE Software for Industrial Equipment, Zhengzhou University, Zhengzhou 450002, China
[4]These authors contributed equally
[5]Lead contact
*Correspondence: xianhu.liu@zzu.edu.cn
https://doi.org/10.1016/j.xcrp.2025.102664

SUMMARY

Bio-derived radiative coolers offer a sustainable alternative to petrochemical materials but struggle with long-term stability. Here, we report a bioplastic cooling metafilm with a bi-continuous architecture engineered through crystallization modulation. The metafilm achieves high solar reflectance (98.7%), exceptional thermal emittance (96.6%), and ultra-low thermal conductivity (0.049 W m^{-1} K^{-1}). It provides a maximum sub-ambient cooling of ∼9.2°C at midday, with an average cooling power of 136 W m^{-2} under peak solar intensity (944.9 W m^{-2}). Notably, it sustains a stable cooling of 5°C–6.5°C even when subjected to severe conditions like prolonged acid (pH 1, 120 h) and ultraviolet (UV; ∼8 months) exposure. This work offers a new strategy for designing sustainable, durable, and energy-efficient cooling materials through structural innovation.

INTRODUCTION

The World Meteorological Organization reported in 2021 that "the last seven years have been the hottest on record," highlighting the severe threat climate change poses to humans, plants, and animals.[1–3] While cooling devices like air conditioners and refrigerators provide comfort, they significantly increase energy consumption and environmental pollution. Passive radiative cooling (PRC) holds great promise for energy savings by enabling cooling without mechanical devices or external energy sources.[4–7] However, several challenges remain.[8,9]

PRC performance is largely governed by the microstructure, where morphological parameters and the refractive index influence light interaction and electromagnetic field strength.[10–13] Intentional tuning of micromorphology emerges as an effective strategy to enhance light scattering. This approach is widely explored, particularly in polymer-based radiative coolers, including controlled-morphology foam,[11] layered porous coatings,[14] shish-kebab superstructure film,[15,16] and nanofiber fabric.[17–19] Despite this, many multilayer materials still exhibit low cooling efficiency.[20,21] Additionally, although ceramic-based nanocomposites and petroleum-derived polymers keep a favorable cooling performance, they also raise environmental concerns, including nanoparticle toxicity to ecosystems and white pollution.[22–26] Bioplastic radiative coolers present a more sustainable alternative—for instance, a recently developed bio-based aerogel derived from DNA and gelatin demonstrates excellent cooling performance.[27] However, its severe solubility and poor weather resistance pose challenges to long-term cooling stability, often necessitating the use of commercial coatings to enhance durability.

As a commercialized bioplastic, poly (lactic acid) (PLA) is undoubtedly a highly promising candidate for the manufacture of radiant coolers.[28] PLA is easy to process and exhibits mechanical properties comparable to petroleum-based polymers.[20] Its distinctive bonding vibrations within the atmospheric transparency window result in strong vibrational absorption bands, making it a promising material for selective thermal emission. Additionally, it can form stereo-complex crystals (SCs) through the alternating arrangement of different molecular chains from poly (L-lactide) (PLLA) and poly (D-lactide) (PDLA).[29–31] SCs possess a melting point approximately 50°C higher than that of homocrystals (HCs) and demonstrate superior mechanical strength, thermal stability, and weathering resistance. The advantage of this strategy lies in its ability to enhance macroscopic properties without impairing the degradability, as PLA-containing SC crystals can still be degraded by enzymatic,[32] hydrolytic,[33] and thermal degradation.[34] Therefore, by optimizing the crystalline structure without relying on surface coatings or nanofillers, it is possible to develop high-performance, environmentally friendly, and durable radiative coolers.

We present a bioplastic cooling metafilm (BPCM) with 98.7% reflectance and 96.6% emittance. By modulating molecular chain states during phase separation and forming SC crystals, BPCM develops a bi-continuous structure that enhances light

Please cite this article in press as: Hou et al., A structural bioplastic metafilm for durable passive radiative cooling, Cell Reports Physical Science (2025), https://doi.org/10.1016/j.xcrp.2025.102664

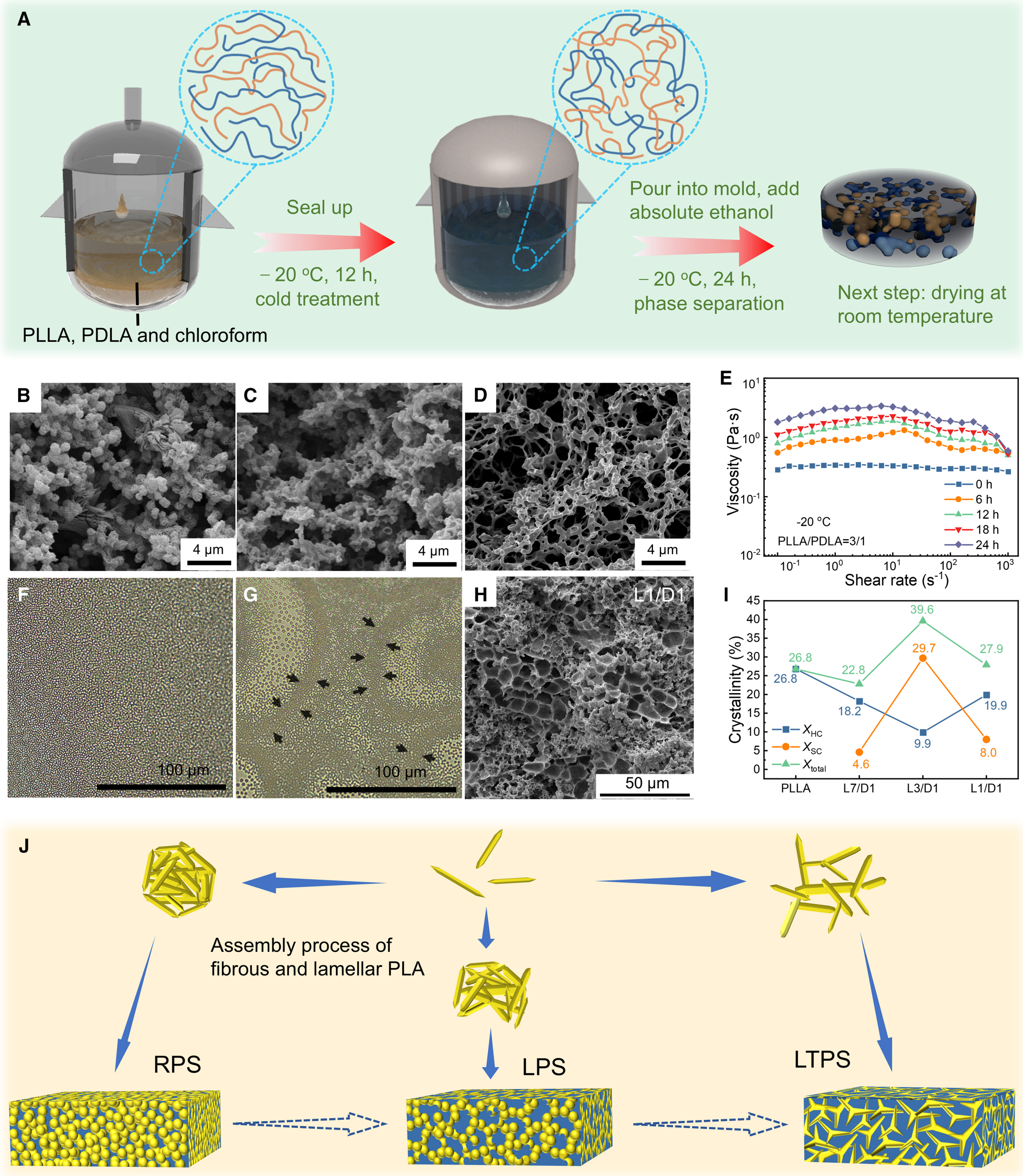

Figure 1. Manufacturing process and structure regulation of BPCM

(A) Preparation of BPCM by LTPS.

(B–D) SEM images of metafilms prepared by room temperature phase separation (RPS), low-temperature phase separation (LPS), and low-temperature two-step phase separation (LTPS). The scale bars represent 4 μm.

(E) Rheological test for precursor solutions.

(legend continued on next page)

Please cite this article in press as: Hou et al., A structural bioplastic metafilm for durable passive radiative cooling, Cell Reports Physical Science (2025), https://doi.org/10.1016/j.xcrp.2025.102664

scattering and resonance. This results in a maximum sub-ambient cooling of ~9.2°C and an average daytime cooling of ~4.9°C. Simulations show that BPCM can reduce building energy consumption by up to 20.3% annually in certain cities. With a high SC content (29.7%), it exhibits excellent thermal stability, acid resistance, and ultraviolet (UV) durability, making it a strong candidate for next-generation eco-friendly radiative coolers.

RESULTS

Manufacturing process and structure regulation

We developed a scalable low-temperature two-step phase separation (LTPS) strategy to fabricate BPCM with a bi-continuous architecture (~500 μm thick; Figures 1A and S1). A homogeneous solution was incubated at −20°C for 12 h, cast into molds with non-solvent additives to induce phase separation, and dried at room temperature, yielding BPCMs with tunable size and morphology. For comparison, BPCMs were also prepared by conventional room temperature (RPS) and direct low-temperature phase separation (LPS) (Note S1; Figure S2). RPS (Figure 1B) produces a metafilm with stacked spherical particles and looser pore clusters. In LPS (Figure 1C), lower temperature suppresses solvent volatilization, extending phase separation and promoting pore development, leading to a bi-continuous structure with less distinct pore features.[35] In contrast, LTPS (Figure 1D) yields a superior bi-continuous reticular architecture.

Compared to RPS and LPS, LTPS includes an additional cold treatment stage for the precursor solution, resembling the inverse of "shear thinning" phenomena (Figure 1E).[36,37] Rheological experiments on solutions with varying cold treatment durations (0, 6, 12, 18, and 24 h) show that the viscosity increases in the low-frequency domain and decreases in the high-frequency spectrum with longer cold treatment, confirming enhanced molecular chain entanglement. An optimal cold treatment duration of 12 h does not cause significant microphase separation (Note S2; Figure S3). This chain entanglement promotes SC crystallization (Note S3; Figure S4), resulting in higher SC crystallinity and larger crystal size in the LTPS process compared to LPS. Larger and more intact SCs typically exhibit fewer structural defects, contributing to their enhanced thermal stability and durability. The increased SC crystallinity and crystal size also reflect improved structural integrity from the molecular to the macroscopic scale.

The PDLA/PLLA ratio significantly affects SC crystallization and microstructure (Figure S5). Pure PLLA forms a honeycomb-like network (6.31-μm pores), while L7/D1 reduces pore size (4.56 μm) with spherical granular synapses. L3/D1 develops a bi-continuous structure with the smallest pores (1.61 μm), and L1/D1 exhibits a hybrid structure with broader pore distribution (Figure 1H). Polarization optical microscope (POM) imaging shows distinct phase boundaries in L1/D1 films (Figure 1G) compared to L3/D1 (Figure 1F), indicating pronounced microphase separation. Wide-angle X-ray diffraction (WAXD) and differential scanning calorimetry (DSC) analyses (Figures 1I and S6–S8; Note S4) show that L3/D1 achieves the highest SC melting point (218.5°C) and crystallinity (29.7%), while L1/D1 drops to 8.0%. Thermal gravimetric analyzer (TGA) results (Figure S9) show L3/D1's superior thermal stability ($T_5\%$ = 340°C), while L1/D1's poor crystallization leads to the lowest $T_5\%$ (315°C).

Based on the above findings, we propose a self-assembly mechanism for the bi-continuous structure (Figure 1J): (1) in RPS, PLA microspheres consist of fibrous and lamellar crystallites formed by the PLA-rich phase[38]; (2) in LPS, low temperature inhibits the enrichment of crystallites, leading to a transition state with defective microspheres and a bi-continuous structure; and (3) in LTPS, enhanced chain entanglement promotes crystallite bridging, forming a more refined bi-continuous rather than microsphere enrichment.

Optical properties and energy-saving simulations

Figure 2A shows that the solar-weighted reflectance of LTPS reaches 98.7%, primarily due to the Mie scattering resonance effect, outperforming RPS (96.7%) and LPS (97.2%) due to the more effective stacking of smaller microspheres. In the 3–20 μm infrared range, LTPS also exhibits excellent emittance of 96.6%. The impact of varying PLLA/PDLA ratios on reflectance and emittance is shown in Figure S10. Increasing the PDLA content enhances the solar reflectance in the 0.3–2.5 μm range, peaking at the L3/D1 ratio. At a 1:1 PLLA/PDLA ratio, pore differentiation increases, leading to larger pore sizes and a slight reduction in reflectance. Emittance in the 8–13 μm infrared band follows a similar trend to solar reflectance, with smaller variations.

Finite-difference time-domain (FDTD) simulations (Figure 2B) further confirm that the porous structure effectively scatters and reflects sunlight (0.3–2.5 μm) when the pore size ranges from 0.5 to 4 μm. Thus, as indicated by the morphological analysis in Figure S5, an insufficient (pure PLLA and L7/D1) or excessive (L1/D1) ratio of PLLA to PDLA prevents the formation of a bi-continuous structure capable of achieving the most effective resonance scattering of sunlight. Additionally, heat from the hot external environment is transferred to the internal space via radiative cooling materials through thermal convection and conduction, making low thermal conductivity essential for efficient radiant cooling. The internal structures of RPS and LPS metafilms are primarily composed of stacked PLA microspheres with limited porosity, resulting in low porosity values of 35.1% and 59.7%, respectively (Figure 2C). In contrast, the LTPS metafilm exhibited high porosity (84.6%), leading to an ultra-low thermal conductivity of 0.049 W m^{-1} K^{-1}.

To evaluate the energy-saving potential of the LTPS metafilm, we employed EnergyPlus to simulate building energy consumption under the climatic conditions of ten representative cities worldwide. Detailed climate information for each city is provided

(F and G) POM images of L3/D1 and L1/D1 metafilms prepared by rapid spin coating. The scale bars represent 100 μm.
(H) Distribution pores of L1/D1. The scale bar represents 50 μm.
(I) HC/SC crystallinity of PLLA, L7/D1, L3/D1, and L1/D1.
(J) Schematic illustration of bi-continuous structure self-assembly.

Please cite this article in press as: Hou et al., A structural bioplastic metafilm for durable passive radiative cooling, Cell Reports Physical Science (2025), https://doi.org/10.1016/j.xcrp.2025.102664

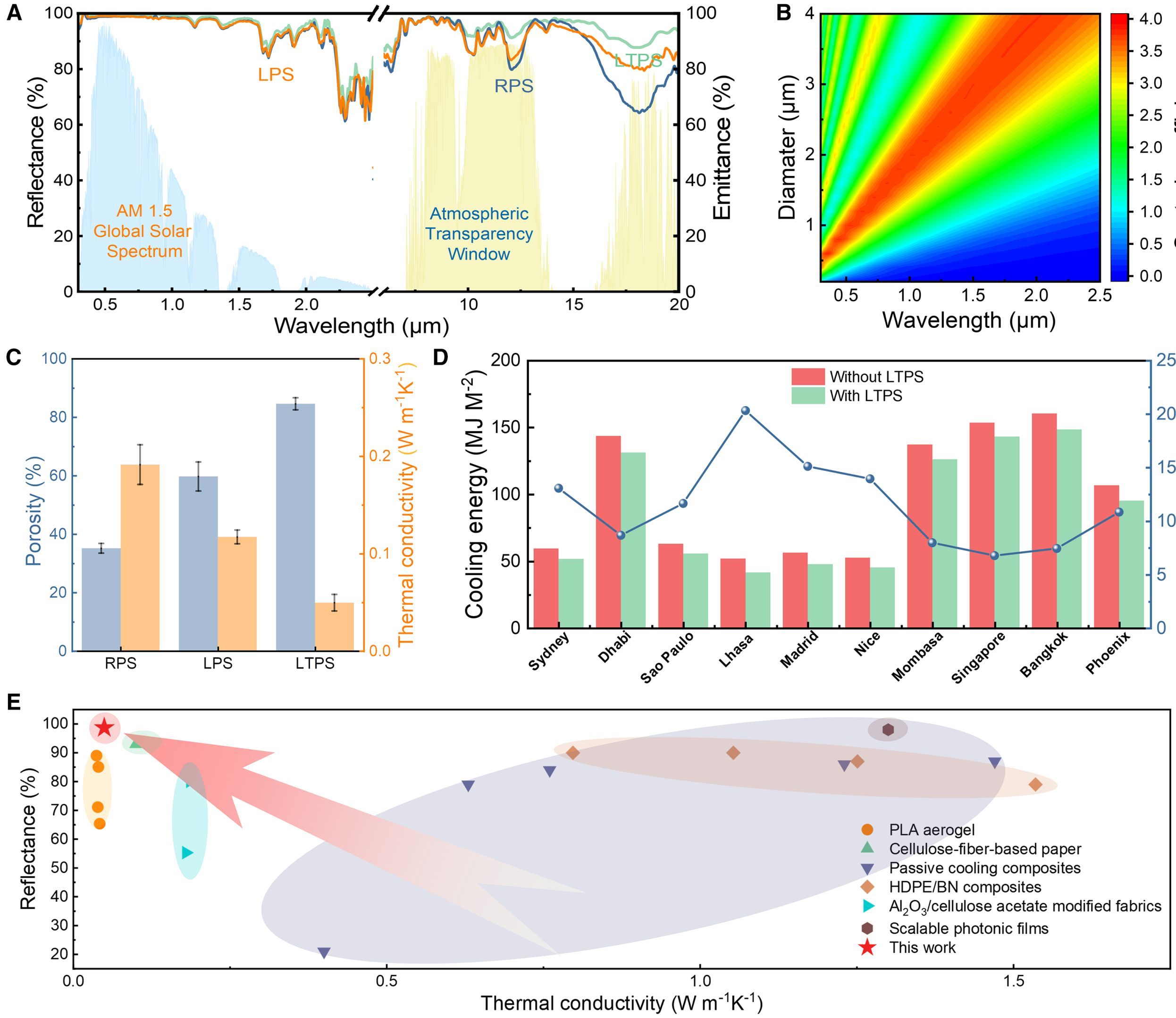

Figure 2. Optical properties and energy-saving simulations of BPCM

(A) Reflectance and emittance spectra of BPCMs.

(B) Theoretical analysis of the pore's scattering efficiency on the incident sunlight.

(C) Porosity and thermal conductivity. Data are represented as mean measurements, and the bars indicate the SD.

(D) Annual cooling energy and energy-saving percentages for different cities.

(E) A comparison between BPCM and other cooling materials reported in previous studies.

in Table S4. The cooling energy savings potential was evaluated by comparing the annual energy consumption of a building model with and without LTPS metafilm wrapping. The results (Figure 2D) show that when the LTPS metafilm is used as the outermost building material, average annual cooling energy consumption is significantly reduced. For instance, simulations for Lhasa, China, indicate that the metafilm can lower the city's annual cooling energy consumption by 20.3%.

Moreover, to emphasize the outstanding performance of PLA metafilms, we have assessed them within the broader context of the field. The developed PLA metafilms demonstrate superior solar reflectivity and low thermal conductivity compared to previously reported radiative coolers, such as PLA aerogels,[39] cellulose-fiber-based paper,[40] passive cooling composites,[41] HDPE/BN composites,[42] Al_2O_3/cellulose acetate-modified fabrics,[43] and scalable photonic films[44] (Figure 2E). This indicates that with skillful structural design, the degradation benefits of PLA can be maintained while achieving superior performance compared to other cooling materials and composites.

Cooling measurements

Figure 3A shows the outdoor radiative cooling test setup for BPCM. The outdoor test was conducted in Zhengzhou City, China (34° 78′ N, 113° 167′ E, May 18, 2024) (Figure 3B). On sunnier days, the LTPS metafilm consistently maintained a temperature lower than the ambient temperature, showcasing its

Please cite this article in press as: Hou et al., A structural bioplastic metafilm for durable passive radiative cooling, Cell Reports Physical Science (2025), https://doi.org/10.1016/j.xcrp.2025.102664

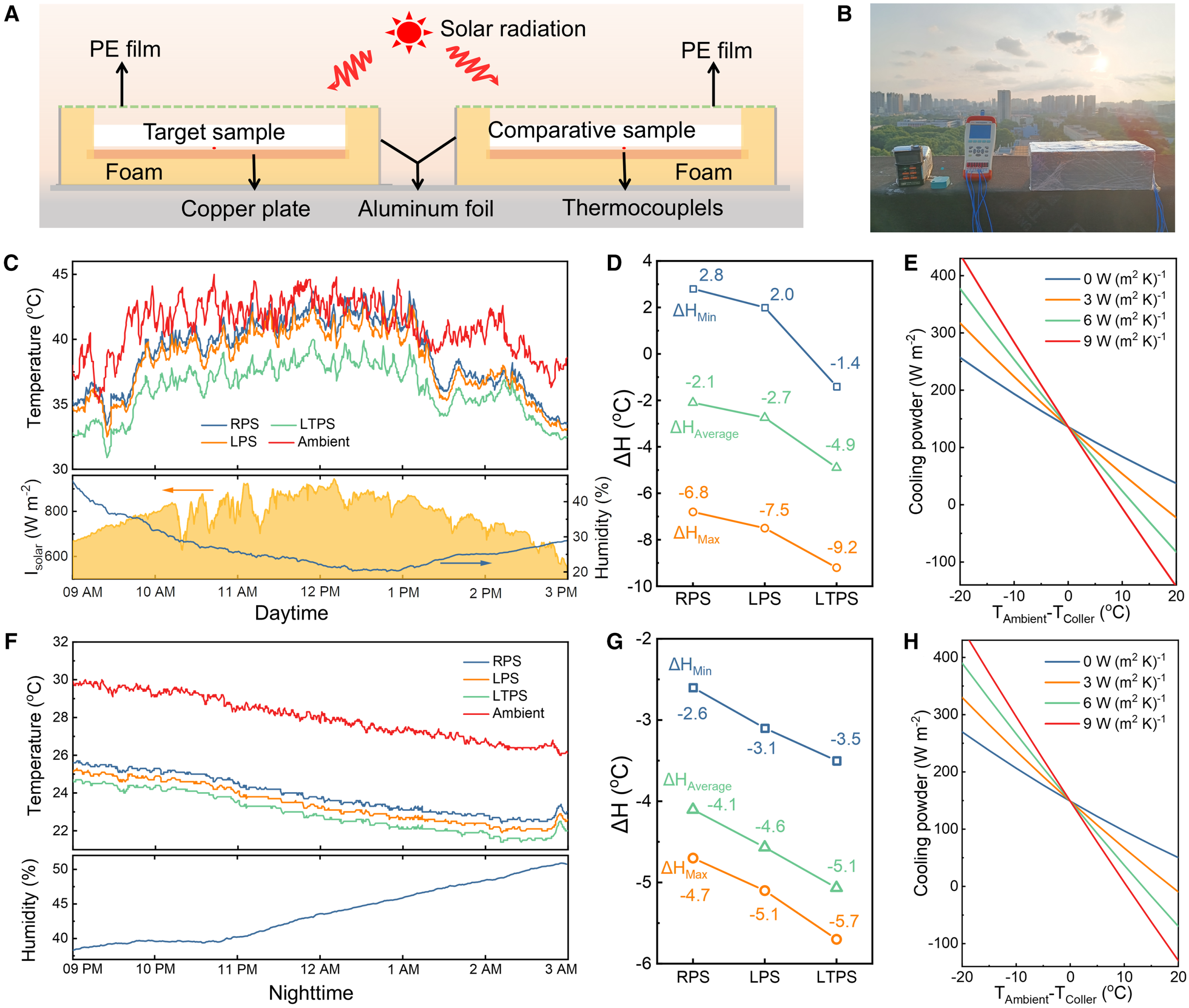

Figure 3. Cooling performance of BPCM

(A) Schematic illustration for the radiative cooling measurement.

(B) Photo of the experimental setup.

(C and F) Temperature measurement of the sub-ambient cooling performance test for daytime and nighttime in Zhengzhou, China.

(D and G) Extracted temperature difference for daytime and nighttime.

(E and H) The calculated cooling power of LTPS at 30°C during the daytime and nighttime (non-radiative heat transfer coefficients [h_c] are 0, 3, 6, and 9 W m^{-2} K^{-1}).

superior radiant cooling performance throughout the day. In contrast, while the RPS and LPS metafilms also exhibited temperatures lower than the ambient temperature, their cooling efficiency was not as high as that of the LTPS metafilm. This can be attributed to the LTPS metafilm's high solar reflectance and strong infrared emission, as well as, more importantly, their high porosity and low thermal conductivity (Figure 3C). In nighttime environments, the LTPS metafilm also maintains stable cooling throughout the entire period (Figure 3F).

Figures 3D and 3G illustrate the typical temperature deviation values from the average ambient temperature for the three BPCMs during daytime and nighttime, respectively. For detailed temperature differences, refer to Figure S11. During daytime and nighttime, the LTPS metafilm exhibited average temperature reductions of 4.9°C and 5.1°C, respectively. In comparison, the RPS metafilm showed reductions of 2.1°C and 4.1°C, while the LPS metafilm demonstrated reductions of 2.7°C and 4.6°C, respectively. The cooling power of LTPS metafilm, considering varying non-radiative coefficients, can be determined using Equation 11. Additionally, the cooling power of both RPS and LPS metafilms has been calculated (Figure S12). In Figures 3E and 3H, the cooling power ($T_{Ambient} - T_{Cooler} = 0$) of the LTPS metafilm was 136 W m^{-2} during the day and 149 W m^{-2} at night, surpassing that of the RPS metafilm (109 and 131 W m^{-2}) and the

Please cite this article in press as: Hou et al., A structural bioplastic metafilm for durable passive radiative cooling, Cell Reports Physical Science (2025), https://doi.org/10.1016/j.xcrp.2025.102664

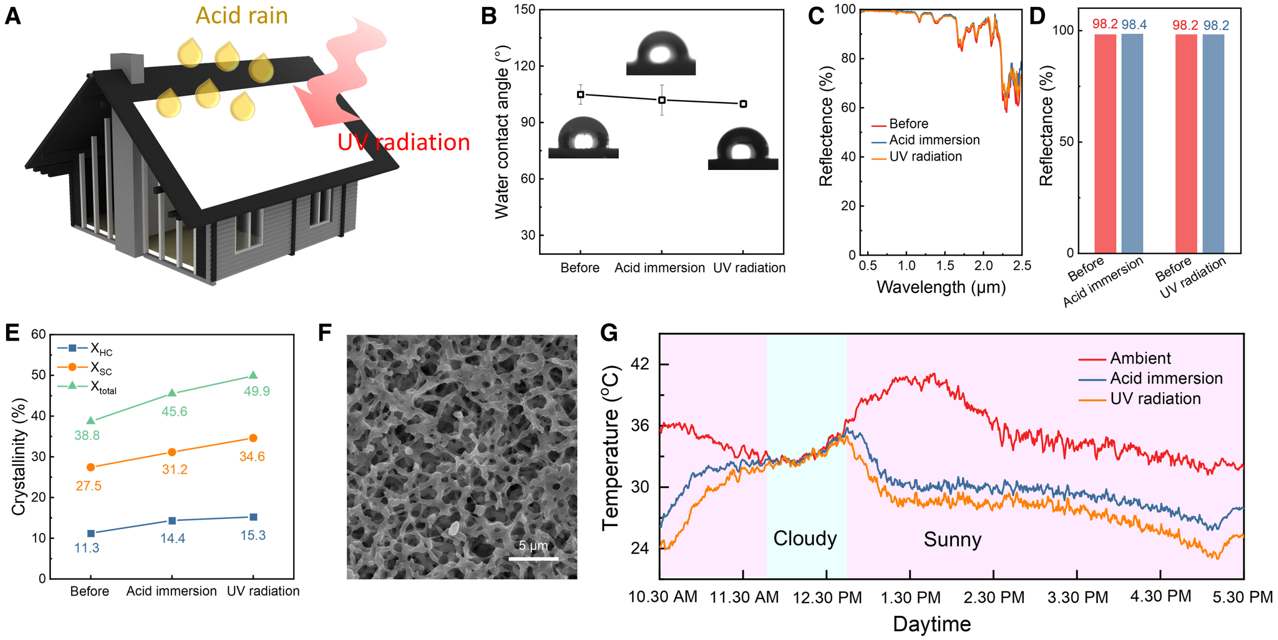

Figure 4. Durability of BPCM

(A) Harsh environmental conditions for outdoor applications of radiative cooling materials.
(B) Water contact angle of BPCM before and after aging. The points are centered on the mean, and the bars indicate the SD.
(C and D) Solar reflectance and average reflectance curves of BPCM before and after aging.
(E) Crystallinity of BPCM before and after aging.
(F) Microscopic morphology of BPCM after UV aging. The scale bar represents 5 μm.
(G) Cooling effect of BPCM after aging.

LPS metafilm (111 and 132 W m^{-2}). These results are consistent with the temperature observations from outdoor tests.

To further examine the impact of microstructure on the cooling performance of BPCM, outdoor temperature tests were conducted on metafilms with varying PLLA/PDLA ratios (Figure S13). Pure PLLA features large, disconnected pore sizes, resulting in consistently higher temperatures than the ambient temperature during the day and less effective cooling at night. L7/D1 is also less effective in daytime and nighttime cooling because of its structural similarity to pure PLLA. In contrast, L3/D1 with reticulated pores and L1/D1 with regionally distributed multilayered pore structures demonstrate excellent radiative cooling performance during both day and night, owing to their high emittance and reflectivity. The average temperature difference between daytime and nighttime for each BPCM is shown in Figure S14. L3/D1 and L1/D1 achieve average cooling of 4.9°C and 4.5°C during the day, both of which are higher than the cooling of the other metafilms. At night, these two metafilms also achieve temperature reductions of 5.0°C and 3.4°C, respectively. These experimental research and theoretical simulations highlight the impressive cooling performance of BPCM. They demonstrate strong efficacy and hold the promise for energy-saving and environmentally friendly applications in building design.

Durability of BPCM

PRC materials are exposed to outdoor conditions and are directly affected by harsh environments, such as acidic rain and intense UV rays (Figure 4A). Therefore, it is crucial to thoroughly assess the acid and UV resistance of BPCM. BPCM was immersed in an acidic solution with a pH of 1 at room temperature for 120 h, followed by natural drying for 48 h. The UV aging test was conducted using a UV weathering tester with the UV-340 standard, simulating 48 h of accelerated aging, equivalent to 8 months of natural exposure. The water wettability of BPCM before and after aging is shown in Figure 4B. The metafilm initially exhibits hydrophobicity with a water contact angle of 105°, which decreases slightly after acid immersion and UV radiation but remains hydrophobic in both cases. Moreover, the solar reflectance of BPCM remains high, showing almost no change after both types of aging (Figures 4C and 4D).

This stability is attributed to its high SC crystal content (Figures 4E and S15). Notably, the HC and SC crystal contents of BPCM increased slightly after acid immersion and UV radiation, rising to 14.4% and 31.2%, respectively, after strong acid immersion and further to 15.3% and 34.6% after UV radiation. This enhanced crystallinity ensures the stability of BPCM's microstructure under acidic conditions and UV exposure. As shown in Figure 4F, the internal bi-continuous structure of BPCM remains intact following UV irradiation tests.

The outdoor test for the sample after aging was conducted in an open grassy field in Adelaide, Australia (34° 52′ S, 138° 30′ E, December 11, 2024), to adapt to the seasonal variations. As shown in Figure 4G, after acid immersion, BPCM maintains an average daytime temperature drop of 5.0°C, while after UV

Please cite this article in press as: Hou et al., A structural bioplastic metafilm for durable passive radiative cooling, Cell Reports Physical Science (2025), https://doi.org/10.1016/j.xcrp.2025.102664

radiation, it sustains a temperature drop of 6.5°C. Additionally, under cloudy conditions, the temperature of the aged BPCM closely matches the ambient temperature, as clouds block and reflect solar and infrared radiation, preventing their escape into space. This outdoor test demonstrated that the aged BPCM consistently maintains a temperature below the ambient under a clear sky and direct sunlight, showcasing its durable and stable radiative cooling performance. Additionally, Table S5 presents a comparison between our BPCM and recent PRC materials. The results highlight our work's integrated superiority in cooling performance, environmental stability, and degradability.

DISCUSSION

We proposed a straightforward yet effective approach to produce a BPCM with a uniformly bi-continuous structure and favorable SC crystallinity of 29.7%. Thanks to its bi-continuous structure, optimized to match the wavelength of sunlight, BPCM achieves an outstanding solar reflectivity of 98.7% and excellent thermal emittance of 96.6%. Additionally, the 84.6% porosity results in an ultra-low thermal conductivity of 0.049 W m^{-1} K^{-1}, effectively minimizing parasitic heat gain from the thermal environment. Outdoor temperature tests demonstrate that BPCM can lower daytime temperatures by up to ~9.2°C, with an average reduction of ~4.9°C. It exhibits excellent durability, maintaining stable cooling performance of 5.0°C–6.5°C even in harsh conditions, such as strongly acidic environments (pH 1, 120 h) and prolonged UV exposure (~8 months). Meanwhile, this research sheds light on the self-assembly mechanism underlying the bi-continuous pore structure in PLLA/PDLA metafilms. This work presents an eco-friendlier alternative to emerging radiative cooling technologies, tackling the paradox of easy biodegradability and superior durability. It contributes a step toward the next generation of sustainable passive cooling devices.

METHODS

Materials

Raw materials: PLLA was purchased from Nature Works (USA), which has a D-isomer content of 2%, a weight-average molecular weight (Mw) of 1.25×10^5 and a number-average molecular weight (Mn) of 1.03×10^5. PDLA (D-isomer content = 98.84%, Mw = 1.2×10^5) was furnished from Shenzhen Ruipu Technology. Before being used, both PLLA and PDLA were dried in a vacuum oven at 70°C for more than 12 h to remove water. All additional chemicals and reagents, including chloroform (>99.0%) and absolute ethanol (>99.8%), were furnished by local suppliers and utilized without further treatment.

Preparation of BPCM

PLLA and PDLA were adopted as raw materials, chloroform as solvent, and absolute ethanol as non-solvent. The detailed procedure of LTPS is displayed in Figure 1. PLLA and PDLA were dissolved in chloroform with a 3:1 mass ratio and agitated for 3 h at room temperature to generate a homogeneous solution at 0.07 g mL^{-1}. The solution was poured into a sealed mold and placed in a refrigerator at −20°C for 12 h. Afterward, absolute ethanol was added dropwise into the solution and then phase separated in the refrigerator at −20°C for 24 h. Finally, the solution was dried in a vacuum oven at room temperature for 48 h to obtain a BPCM. Moreover, more metafilms were prepared using LTPS at a precursor concentration of 0.07 g mL^{-1} with varying PLLA/PDLA ratios. These metafilms, containing X wt % PLLA and Y wt % PDLA, were labeled as LX/DY. Among them, the preparation conditions and formulations of the L3/D1 and LTPS metafilm are identical.

Microstructure characterization

At an accelerating voltage of 15 kV, the cross-section micromorphology of BPCM was comprehensively viewed by a field emission scanning electron microscope (FE-SEM; JSM-7001F). All samples were immersed in liquid nitrogen in advance and quickly fractured to produce neat cross-sections. Prior to SEM observation, each cross-section was sputtered with a thin layer of gold to improve conductivity. To calculate pore size distribution and average pore size, more than 100 pores of each SEM image were counted and analyzed using ImageJ software. The average pore size was calculated using Equation 1,[45]

$$D = \frac{\sum D_i N_i}{\sum N_i}, \qquad \text{(Equation 1)}$$

where N_i is the number of pores with a diameter of D_i, assuming that the pore shape is spherical.

Employing a spin-coating method, the cold-treated precursor solutions were used to generate a series of films. They were utilized to study the microphase separation of PLLA and PDLA by an atomic force microscope (AFM; Bruker Multi Mode 8) and a POM (Olympus BX53M). Based on the research of Liu et al.,[46] the solution was uniformly coated on a neat glass slide (2 cm in diameter) at 6,000 rpm. At this rate, the microphase separation of molecular chains during solvent volatilization was effectively suppressed (solvent quenching phenomenon). The spin-coated films with solutions of different cold treatments were studies using an AFM in a tapping mode (Tap300Al-G silicon probes; tip radius: <10 nm; spring constant: 40 N m^{-1}; frequency: 300 kHz). For the films prepared from the solutions with different PLLA/PDLA ratios, their surface morphologies were characterized by a POM.

Crystalline structure characterization

WAXD (wavelength 0.154 nm) was used to determine the crystallinity and crystallite size of BPCM. The distance between the sample and the detector was maintained at 85 mm. Moreover, the operating current, accelerating voltage, and continuous scanning angle were 1,000 μA, 50 kV, and 5°–30°, respectively.

The crystalline and amorphous peaks of WAXD curves can be fitted by the function

$$I(2\theta) = I_{max} \exp\left[\frac{-\pi(2\theta - 2\theta_0)^2}{\beta^2}\right], \qquad \text{(Equation 2)}$$

Please cite this article in press as: Hou et al., A structural bioplastic metafilm for durable passive radiative cooling, Cell Reports Physical Science (2025), https://doi.org/10.1016/j.xcrp.2025.102664

where $I\ (2\theta)$ is the scattering intensity of function 2θ, I_{max} is the maximum peak, $2\theta_0$ is the peak center, and β is the integral width of the peak. X_{total} can be calculated by the following formula[47]:

$$X_{total} = \frac{\sum A_{hkl}}{\sum A_{hkl}+A_{amorphous}}, \quad \text{(Equation 3)}$$

where A_{hkl} is the area of crystalline diffraction peak and $A_{amorphous}$ is the area of amorphous peak. Crystallinities of SCs and HCs were estimated from the diffraction area of corresponding polymorph by[29]

$$X_{SC} = \frac{A_{SC}}{A_{SC}+A_{HC}}X_{total} \text{ and} \quad \text{(Equation 4)}$$

$$X_{HC} = \frac{A_{HC}}{A_{SC}+A_{HC}}X_{total}, \quad \text{(Equation 5)}$$

where A_{SC} and A_{HC} are the diffraction peak areas of SCs and HCs by peak fitting. Scherrer's formula was used to compute the crystallite size of each plane in the WAXD diffraction peaks[48]:

$$D_{hkl} = \frac{K\lambda}{\beta_{hkl}\cos\theta_{hkl}}, \quad \text{(Equation 6)}$$

where D_{hkl} is the crystallite diameter (hkl), K is the Scherrer constant ($K = 0.89$), λ (the wavelength of the X-ray) is 0.154 nm, β_{hkl} is the full width of the diffraction line at half-maximum intensity measured in radians, and θ_{hkl} is the Bragg angle.

Thermal behavior characterization

DSC Q 2000 (TA Instruments, USA) was used to characterize the thermal melting behavior of crystals in BPCM. The testing was conducted in a nitrogen atmosphere to prevent thermal degradation. BPCM (3–5 mg) was placed into an aluminum crucible and kept at 40°C for 3 min to eliminate the thermal history and then heated to 250°C at a rate of 10°C min^{-1}. A TGA (Pyris 1, PerkinElmer, USA) was utilized to profile the thermal degradation behavior of BPCM. The testing was conducted in a nitrogen atmosphere with a temperature increase interval of 50°C–500°C and a rate of 20°C min^{-1}.

Thermal conductivity and porosity characterization

A thermal conductivity meter (Hot Disk TPS2500S) was used to characterize the thermal conductivity of the PLA aerogel by placing the probe in the middle of two identical PLA aerogels and placing a heavy weight on the aerogel to ensure close contact between the probe and the sample.

The porosity (ϕ) is defined as follows:

$$\phi = \frac{(\omega_0 - \omega)\rho}{\rho\omega_0+(\rho_0 - \rho)\omega}\times 100\%, \quad \text{(Equation 7)}$$

where ω_0 and ω represent the masses of the BPCM saturated with ethanol and after ethanol removal, respectively. ρ_0 and ρ denote the densities of ethanol and PLA, respectively.

Outdoor testing, optical performance, and cooling power calculation

An 8-channel K thermocouple (China Yili Technology) was used to simultaneously record the temperatures of the coolers and ambient environment. Solar reflectance spectra (0.3–2.5 μm) were measured using a PTFE integrating sphere and a UV-visible near-infrared (UV-vis-NIR) spectrophotometer (PerkinElmer Lambda 1050). In the infrared range (3–20 μm), spectral reflectivity ($R(\lambda)$) and transmission ($T(\lambda)$) were measured using a Fourier transform infrared spectrometer (FTIR spectrometer; Bruker INVENIOR) equipped with a gold integrating sphere (Bruker A562). The average solar reflectance ($\overline{R}_{solar}$) and emissivity within the atmospheric transparent window ($\overline{\varepsilon}_{ATW}$) for the aerogels are defined as follows:

$$\overline{R}_{\text{solar}} = \frac{\int_{0.3\mu m}^{2.5\mu m} I_{solar}(\lambda)\cdot R_{solar}(\lambda)d\lambda}{\int_{0.3\mu m}^{2.5\mu m} I_{solar}(\lambda)d\lambda} \text{ and} \quad \text{(Equation 8)}$$

$$\overline{\varepsilon}_{ATW} = \frac{\int_{8\mu m}^{13\mu m} I_{BB}(\lambda)\cdot\varepsilon_{ATW}(\lambda)d\lambda}{\int_{8\mu m}^{13\mu m} I_{BB}^{m}(\lambda)d\lambda}, \quad \text{(Equation 9)}$$

where λ represents the solar wavelength and $I_{solar}\ (\lambda)$ is the ASTM G173-03 global solar intensity spectrum (AM1.5).

$$I_{BB}(T,\lambda) = \frac{2hc^2}{\lambda^5 e^{\frac{hc}{T\lambda K_B}-1}}, \quad \text{(Equation 10)}$$

where $I_{BB}\ (T,\ \lambda)$ is the spectral irradiance of a blackbody at temperature T. $R_{\text{solar}}\ (\lambda)$ and $\varepsilon_{ATW}(\lambda)$ denote the spectral reflectivity (0.3–2.5 μm) and spectral thermal emittance (8–13 μm) of the PLA aerogels. The cooling power is defined as follows:

$$P_{cooling} = P_{rad}(T) - P_{sun} - P_{atm}(T_{amb}) - P_{non-rad}, \quad \text{(Equation 11)}$$

where $P_{rad}\ (T)$ represents the radiative power of the PLA cooler at temperature T, P_{sun} refers to the solar irradiance absorbed by the cooler, $P_{atm}\ (T_{amb})$ is the atmospheric thermal radiation absorbed by the cooler, and $P_{non\text{-}rad}$ accounts for non-radiative losses due to convection and conduction. T_{amb} represents the ambient temperature.

$P_{rad}\ (T)$ is the power radiated out by the radiative cooler at temperature T, which can be defined as

$$P_{rad}(T) = 2\pi\int_0^{\frac{\pi}{2}} d\theta\sin\theta\cos\theta\int_{2.5\mu m}^{25\mu m} I_{BB}(T,\lambda)\varepsilon(\lambda,\theta)d\lambda, \quad \text{(Equation 12)}$$

Please cite this article in press as: Hou et al., A structural bioplastic metafilm for durable passive radiative cooling, Cell Reports Physical Science (2025), https://doi.org/10.1016/j.xcrp.2025.102664

where ε (λ, θ) represents the cooler's spectral and angular emissivity. h is Planck's constant, c is the speed of light, and K_B is the Boltzmann constant.

$P_{atm}(T_{amb})$ is the power atmospheric thermal radiation absorbed by the radiant cooler, which can be defined as follows:

$$P_{atm}(T_{amb}) = 2\pi \int_{0}^{\frac{\pi}{2}} d\theta \sin\theta \cos\theta \int_{2.5\mu m}^{25\mu m} I_{BB}^{m}(T,\lambda)\varepsilon(\lambda,\theta)\varepsilon_{atm}(\lambda,\theta)d\lambda, \quad \text{(Equation 13)}$$

where ε_{atm} (λ, θ) is the spectral and angular emissivity of the atmosphere, which can be defined as ε_{atm} (λ, θ) = 1 − $t(\lambda)^{1/\cos\theta}$. $t(\lambda)$ denotes the atmospheric transmittance in the zenithal direction, which can be acquired from the mid-latitude summer atmosphere model (MODTRAN [spectral.com]).

P_{sun} and $P_{non\text{-}rad}$ refer to the power of the solar irradiance absorbed by the cooler and the non-radiant loss caused by convection and conduction, respectively, which can be defined as follows:

$$P_{sun} = \int_{0.3\mu m}^{2.5\mu m} I_{solar}(\lambda)\varepsilon(\lambda,0)d\lambda \text{ and} \quad \text{(Equation 14)}$$

$$P_{non-rad} = h_c(T_{amb} - T), \quad \text{(Equation 15)}$$

where h_c is the non-radiant heat coefficient and T_{amb} and T are the ambient temperature and radiative cooler temperature, respectively.

Acid and UV aging experiments

The sample was immersed in an acidic solution with a pH of 1 at room temperature for 120 h, followed by drying at room temperature for 48 h. The pH measurement was supplied by Shanghai Yidian Scientific Instrument.

UV accelerated aging experiments were conducted using a UVB irradiation light source with a central wavelength of 340 nm and a power of 40 W, installed in a Shanghai LINFENG UV aging test chamber (model: LRHS-NZY, LinPin, Shanghai).

$$Q_h = \frac{Q_{year}}{365 \cdot 24} \text{ and} \quad \text{(Equation 16)}$$

$$D_{outdoor} = \frac{T_{set}Q_a}{T_{anb}Q_h} \cdot 1.5, \quad \text{(Equation 17)}$$

Where $D_{outdoor}$ is the equivalent number of outdoor exposure days per 24 h of accelerated aging, T_{set} (60°C) is the temperature of the UV aging chamber, T_{amb} (16.6°C) is the annual average ambient temperature in Zhengzhou, Q_a (0.76 kW m^{-2}) is the irradiance of the UV lamp, and Q_h (0.14 kW m^{-2}) is the average solar irradiance per hour based on the annual total of 1225 kWh m^{-2} in Zhengzhou. The factor 1.5 is a commonly used empirical acceleration factor in polymer aging studies.

According to the above formula, 48 h of accelerated UV exposure corresponds to approximately 60 days of continuous sunlight. Assuming a natural scenario of 6–8 h of effective sunlight per day, this is equivalent to roughly 6–8 months of real-world outdoor exposure.

RESOURCE AVAILABILITY

Lead contact

Further information and requests for resources and materials should be directed to and will be fulfilled by the lead contact, Prof. Xianhu Liu (xianhu.liu@zzu.edu.cn).

Materials availability

This study did not generate new unique materials.

Data and code availability

- The article includes all data generated or analyzed during this study. Detailed experimental procedures and data are provided in the methods and supplemental information.
- No code was generated in this study.
- Any additional information required to reanalyze the data reported in this paper is available from the lead contact upon request.

ACKNOWLEDGMENTS

The authors thank the National Natural Science Foundation of China (52403055) and the Natural Science Foundation of Henan (242300421010).

AUTHOR CONTRIBUTIONS

Writing – original draft, Y.H.; writing – review & editing, Y.P., X.L., J.M., C.L., and C.S.; investigation, Y.H. and Y.P.; formal analysis, Y.H., Y.P., and J.M.; conceptualization, Y.H. and X.L.; supervision, X.L.; funding acquisition, C.L.

DECLARATION OF INTERESTS

The authors declare no competing interests.

DECLARATION OF GENERATIVE AI AND AI-ASSISTED TECHNOLOGIES

The authors employed AI to enhance the language and readability of this paper. They assume full responsibility and accountability for all the content in this work.

SUPPLEMENTAL INFORMATION

Supplemental information can be found online at https://doi.org/10.1016/j.xcrp.2025.102664.

Received: April 4, 2025
Revised: May 5, 2025
Accepted: May 29, 2025

REFERENCES

1. Armstrong McKay, D.I., Staal, A., Abrams, J.F., Winkelmann, R., Sakschewski, B., Loriani, S., Fetzer, I., Cornell, S.E., Rockström, J., and Lenton, T.M. (2022). Exceeding 1.5 degrees C global warming could trigger multiple climate tipping points. Science *377*, eabn7950. https://doi.org/10.1126/science.abn7950.
2. Lenton, T.M., Xu, C., Abrams, J.F., Ghadiali, A., Loriani, S., Sakschewski, B., Zimm, C., Ebi, K.L., Dunn, R.R., Svenning, J.C., and Scheffer, M. (2023). Quantifying the human cost of global warming. Nat. Sustain. *6*, 1237–1247. https://doi.org/10.1038/s41893-023-01132-6.

3. Wunderling, N., Winkelmann, R., Rockström, J., Loriani, S., Armstrong McKay, D.I., Ritchie, P.D.L., Sakschewski, B., and Donges, J.F. (2022). Global warming overshoots increase risks of climate tipping cascades in a network model. Nat. Clim. Change *13*, 75–82. https://doi.org/10.1038/s41558-022-01545-9.

4. Woods, J., James, N., Kozubal, E., Bonnema, E., Brief, K., Voeller, L., and Rivest, J. (2022). Humidity's impact on greenhouse gas emissions from air conditioning. Joule *6*, 726–741. https://doi.org/10.1016/j.joule.2022.02.013.

5. Pérez-Lombard, L., Ortiz, J., and Pout, C. (2008). A review on buildings energy consumption information. Energy Build. *40*, 394–398. https://doi.org/10.1016/j.enbuild.2007.03.007.

6. Huang, M.C., Yang, M., Guo, X.J., Xue, C.H., Wang, H.D., Ma, C.Q., Bai, Z., Zhou, X., Wang, Z., Liu, B.Y., et al. (2023). Scalable multifunctional radiative cooling materials. Prog. Mater. Sci. *137*, 101144. https://doi.org/10.1016/j.pmatsci.2023.101144.

7. Sakata, P., Muangnapoh, K., Rueangsawang, W., Ponghiransmith, C., Pornmanat, C., Phuphathanaphong, N., Mangthong, P., Kaewkhao, J., Suttiruengwong, S., and Kanjanaboos, P. (2024). Radiative cooling film enabled by droplet-like infrared hot spots via low-cost and scalable spray-coating process for tropical regions. Cell Rep. Phys. Sci. *5*, 101899. https://doi.org/10.1016/j.xcrp.2024.101899.

8. Liang, J., Wu, J., Guo, J., Li, H., Zhou, X., Liang, S., Qiu, C.W., and Tao, G. (2023). Radiative cooling for passive thermal management towards sustainable carbon neutrality. Natl. Sci. Rev. *10*, nwac208. https://doi.org/10.1093/nsr/nwac208.

9. Zhao, D., and Tang, H. (2023). Staying stably cool in the sunlight. Science *382*, 644–645. https://doi.org/10.1126/science.adk9614.

10. Zhou, L., Song, H., Liang, J., Singer, M., Zhou, M., Stegenburgs, E., Zhang, N., Xu, C., Ng, T., Yu, Z., et al. (2019). A polydimethylsiloxane-coated metal structure for all-day radiative cooling. Nat. Sustain. *2*, 718–724. https://doi.org/10.1038/s41893-019-0348-5.

11. Wang, Y., Wang, T., Liang, J., Wu, J., Yang, M., Pan, Y., Hou, C., Liu, C., Shen, C., Tao, G., and Liu, X. (2023). Controllable-morphology polymer blend photonic metafoam for radiative cooling. Mater. Horiz. *10*, 5060–5070. https://doi.org/10.1039/D3MH01008B.

12. Wang, T., Wu, Y., Shi, L., Hu, X., Chen, M., and Wu, L. (2021). A structural polymer for highly efficient all-day passive radiative cooling. Nat. Commun. *12*, 365. https://doi.org/10.1038/s41467-020-20646-7.

13. Wu, X., Li, J., Xie, F., Wu, X.E., Zhao, S., Jiang, Q., Zhang, S., Wang, B., Li, Y., Gao, D., et al. (2024). A dual-selective thermal emitter with enhanced subambient radiative cooling performance. Nat. Commun. *15*, 815. https://doi.org/10.1038/s41467-024-45095-4.

14. Mandal, J., Fu, Y., Overvig, A.C., Jia, M., Sun, K., Shi, N.N., Zhou, H., Xiao, X., Yu, N., and Yang, Y. (2018). Hierarchically porous polymer coatings for highly efficient passive daytime radiative cooling. Science *362*, 315–319. https://doi.org/10.1126/science.aat9513.

15. Liu, X., Li, Y., Pan, Y., Zhou, Z., Zhai, Z., Liu, C., and Shen, C. (2023). A shish-kebab superstructure film for personal radiative cooling. ACS Appl. Mater. Interfaces *15*, 17188–17194. https://doi.org/10.1021/acsami.3c00120.

16. Yang, R., Xie, F., Li, Y., Wang, X., Pan, Y., Liu, C., Shen, C., and Liu, X. (2024). Advancing thermal comfort: an innovative SiO_2 microsphere-decorated shish-kebab film composite for enhanced personal cooling. Advanced Nanocomposites *1*, 86–93. https://doi.org/10.1016/j.adna.2024.02.001.

17. Li, D., Liu, X., Li, W., Lin, Z., Zhu, B., Li, Z., Li, J., Li, B., Fan, S., Xie, J., and Zhu, J. (2021). Scalable and hierarchically designed polymer film as a selective thermal emitter for high-performance all-day radiative cooling. Nat. Nanotechnol. *16*, 153–158. https://doi.org/10.1038/s41565-020-00800-4.

18. Cai, L., Peng, Y., Xu, J., Zhou, C., Zhou, C., Wu, P., Lin, D., Fan, S., and Cui, Y. (2019). Temperature regulation in colored infrared-transparent polyethylene textiles. Joule *3*, 1478–1486. https://doi.org/10.1016/j.joule.2019.03.015.

19. Liu, R., Zhao, S., Wu, X., Zhao, Z., Wang, K., Guo, Z., Xi, A., Lan, F., Li, R., Liu, R., et al. (2025). Radiative cooling meta-fabric integrated with knitting perspiration-wicking and coating heat conduction. ACS Nano *19*, 826–836. https://doi.org/10.1021/acsnano.4c12196.

20. Zeng, S., Pian, S., Su, M., Wang, Z., Wu, M., Liu, X., Chen, M., Xiang, Y., Wu, J., Zhang, M., et al. (2021). Hierarchical-morphology metafabric for scalable passive daytime radiative cooling. Science *373*, 692–696. https://doi.org/10.1126/science.abi5484.

21. Wu, X., Li, J., Jiang, Q., Zhang, W., Wang, B., Li, R., Zhao, S., Wang, F., Huang, Y., Lyu, P., et al. (2023). An all-weather radiative human body cooling textile. Nat. Sustain. *6*, 1446–1454. https://doi.org/10.1038/s41893-023-01200-x.

22. Lin, K., Chen, S., Zeng, Y., Ho, T.C., Zhu, Y., Wang, X., Liu, F., Huang, B., Chao, C.Y.-H., Wang, Z., and Tso, C.Y. (2023). Hierarchically structured passive radiative cooling ceramic with high solar reflectivity. Science *382*, 691–697. https://doi.org/10.1126/science.adi4725.

23. Zhao, X., Li, T., Xie, H., Liu, H., Wang, L., Qu, Y., Li, S.C., Liu, S., Brozena, A.H., Yu, Z., et al. (2023). A solution-processed radiative cooling glass. Science *382*, 684–691. https://doi.org/10.1126/science.adi2224.

24. MacLeod, M., Arp, H.P.H., Tekman, M.B., and Jahnke, A. (2021). The global threat from plastic pollution. Science *373*, 61–65. https://doi.org/10.1126/science.abg5433.

25. Wang, Y.L., Lee, Y.H., Chou, C.L., Chang, Y.S., Liu, W.C., and Chiu, H.W. (2024). Oxidative stress and potential effects of metal nanoparticles: A review of biocompatibility and toxicity concerns. Environ. Pollut. *346*, 123617. https://doi.org/10.1016/j.envpol.2024.123617.

26. Li, X., Peoples, J., Huang, Z., Zhao, Z., Qiu, J., and Ruan, X. (2020). Full daytime sub-ambient radiative cooling in commercial-like paints with high figure of merit. Cell Rep. Phys. Sci. *1*, 100221. https://doi.org/10.1016/j.xcrp.2020.100221.

27. Ma, J.W., Zeng, F.R., Lin, X.C., Wang, Y., Ma, Y.H., Jia, X.X., Wang, Y.Q., Liu, B.W., Wang, Y., and Zhao, H.B. (2024). A photoluminescent hydrogen-bonded biomass aerogel for sustainable radiative cooling. Science *385*, 68–74. https://doi.org/10.1126/science.adn5694.

28. Shen, C., and Liu, X. (2024). DNA and gelatin—a cool aerogel mix. Science *385*, 30. https://doi.org/10.1126/science.adq5190.

29. Xie, Q., Bao, J., Shan, G., Bao, Y., and Pan, P. (2019). Fractional crystallization kinetics and formation of metastable β-form homocrystals in poly(l-lactic acid)/poly(d-lactic acid) racemic blends induced by precedingly formed stereocomplexes. Macromolecules *52*, 4655–4665. https://doi.org/10.1021/acs.macromol.9b00644.

30. Bai, D., Liu, H., Bai, H., Zhang, Q., and Fu, Q. (2017). Low-temperature sintering of stereocomplex-type polylactide nascent powder: effect of crystallinity. Macromolecules *50*, 7611–7619. https://doi.org/10.1021/acs.macromol.7b01794.

31. Hou, Y., Jia, H., Pan, Y., Liu, C., Shen, C., and Liu, X. (2023). Porous poly(l-lactide)/poly(d-lactide) blend film with enhanced flexibility and heat resistance via constructing a regularly oriented pore structure. Macromolecules *56*, 7606–7616. https://doi.org/10.1021/acs.macromol.3c01296.

32. Fundador, N.G.V., Takemura, A., and Iwata, T. (2011). Structural properties and enzymatic degradation behavior of PLLA and stereocomplexed PLA nanofibers. Macromol. Mater. Eng. *295*, 865–871. https://doi.org/10.1002/mame.201000197.

33. Andersson, S.R., Hakkarainen, M., Inkinen, S., Södergård, A., and Albertsson, A.C. (2012). Customizing the hydrolytic degradation rate of stereocomplex PLA through different PDLA architectures. Biomacromolecules *13*, 1212–1222. https://doi.org/10.1021/bm300196h.

34. Fan, Y., Nishida, H., Shirai, Y., Tokiwa, Y., and Endo, T. (2004). Thermal degradation behaviour of poly(lactic acid) stereocomplex. Polym. Degrad. Stabil. *86*, 197–208. https://doi.org/10.1016/j.polymdegradstab.2004.03.001.

35. Sun, X., Guo, Y., Wang, R., Tang, H., Wang, L., and Qin, S. (2022). Flexure-resistant and additive-free poly (L-lactic acid) hydrophobic membranes fabricated by slow phase separation. Int. J. Biol. Macromol. *209*, 1605–1612. https://doi.org/10.1016/j.ijbiomac.2022.04.051.

36. Xu, Z., Sun, R., Lu, W., Patil, S., Mays, J., Schweizer, K.S., and Cheng, S. (2022). Nature of steady-state fast flow in entangled polymer melts: chain stretching, shear thinning, and viscosity scaling. Macromolecules *55*, 10737–10750. https://doi.org/10.1021/acs.macromol.2c01345.

37. Yan, Z.C., Costanzo, S., Jeong, Y., Chang, T., and Vlassopoulos, D. (2016). Linear and nonlinear shear rheology of a marginally entangled ring polymer. Macromolecules *49*, 1444–1453. https://doi.org/10.1021/acs.macromol.5b02651.

38. Wang, Y., Yang, H., Chen, Z., Chen, N., Pang, X., Zhang, L., Minari, T., Liu, X., Liu, H., and Chen, J. (2018). Recyclable oil-absorption foams via secondary phase separation. ACS Sustain. Chem. Eng. *6*, 13834–13843. https://doi.org/10.1021/acssuschemeng.8b01950.

39. Liu, X., Zhang, M., Hou, Y., Pan, Y., Liu, C., and Shen, C. (2022). Hierarchically superhydrophobic stereo-complex poly (lactic acid) aerogel for daytime radiative cooling. Adv. Funct. Mater. *32*, 2207414. https://doi.org/10.1002/adfm.202207414.

40. Tian, Y., Shao, H., Liu, X., Chen, F., Li, Y., Tang, C., and Zheng, Y. (2021). Superhydrophobic and recyclable cellulose-fiber-based composites for high-efficiency passive radiative cooling. ACS Appl. Mater. Interfaces *13*, 22521–22530. https://doi.org/10.1021/acsami.1c04046.

41. Yang, Z., Zhou, Z., Sun, H., Chen, T., and Zhang, J. (2021). Construction of a ternary channel efficient passive cooling composites with solar-reflective, thermoemissive, and thermoconductive properties. Compos. Sci. Technol. *207*, 108743. https://doi.org/10.1016/j.compscitech.2021.108743.

42. Wang, Y., Zhang, W., Feng, M., Qu, M., Cai, Z., Yang, G., Pan, Y., Liu, C., Shen, C., and Liu, X. (2022). The influence of boron nitride shape and size on thermal conductivity, rheological and passive cooling properties of polyethylene composites. Compos. Part A Appl. Sci. Manuf. *161*, 107117. https://doi.org/10.1016/j.compositesa.2022.107117.

43. Wei, W., Zhu, Y., Li, Q., Cheng, Z., Yao, Y., Zhao, Q., Zhang, P., Liu, X., Chen, Z., Xu, F., and Gao, Y. (2020). An Al_2O_3-cellulose acetate-coated textile for human body cooling. Sol. Energy Mater. Sol. Cells *211*, 110525. https://doi.org/10.1016/j.solmat.2020.110525.

44. Li, P., Wang, A., Fan, J., Kang, Q., Jiang, P., Bao, H., and Huang, X. (2021). Thermo-optically designed scalable photonic films with high thermal conductivity for subambient and above-ambient radiative cooling. Adv. Funct. Mater. *32*, 2109542. https://doi.org/10.1002/adfm.202109542.

45. Ren, Q., Wu, M., Li, W., Zhu, X., Zhao, Y., Wang, L., and Zheng, W. (2021). A green fabrication method of poly (lactic acid) perforated membrane via tuned crystallization and gas diffusion process. Int. J. Biol. Macromol. *182*, 1037–1046. https://doi.org/10.1016/j.ijbiomac.2021.04.105.

46. Liu, J., Qi, X., Feng, Q., and Lan, Q. (2020). Suppression of phase separation for exclusive stereocomplex crystallization of a high-molecular-weight racemic poly(l-lactide)/poly(d-lactide) blend from the glassy state. Macromolecules *53*, 3493–3503. https://doi.org/10.1021/acs.macromol.0c00112.

47. Huang, Y.F., Zhang, Z.C., Li, Y., Xu, J.Z., Xu, L., Yan, Z., Zhong, G.J., and Li, Z.M. (2018). The role of melt memory and template effect in complete stereocomplex crystallization and phase morphology of polylactides. Cryst. Growth Des. *18*, 1613–1621. https://doi.org/10.1021/acs.cgd.7b01562.

48. Liu, X., Dai, K., Hao, X., Zheng, G., Liu, C., Schubert, D.W., and Shen, C. (2013). Crystalline structure of injection molded β-isotactic polypropylene: analysis of the oriented shear zone. Ind. Eng. Chem. Res. *52*, 11996–12002. https://doi.org/10.1021/ie401162c.

Cell Reports Physical Science, Volume *6*

Supplemental information

A structural bioplastic metafilm for durable passive radiative cooling

Yangzhe Hou, Yamin Pan, Xianhu Liu, Jun Ma, Chuntai Liu, and Changyu Shen

Supplementary Notes

Note S1: Fabrication of BPCM via room-temperature and low-temperature phase separation

For microarchitecture comparison, two more BPCMs were prepared using traditional room-temperature phase separation (RPS) and low-temperature phase separation (LPS) (Figure S2). The former required immediately dropping absolute ethanol into the solution without the cold treatment and then placing it at room temperature for phase separation (Figure S2A); the later involved directly adding absolute ethanol and placing it at -20 ^{o}C for phase separation (Figure S2B). Both were dried to produce metafilms in the same manner as LTPS.

Note S2: AFM images of solution spin-coated films

The film formed by non-cold-treated solution exhibits featureless surface morphology (Figure S3A). However, when the cold treatment time reaches 24 h, the number of phases-separated domains rises (Figure S3B). The findings indicate that the prolonged cold treatment duration, specifically at 24 h, induces a pronounced microphase separation (Figure S3C). Conversely, an optimal cold treatment duration of 12 h does not yield any significant microphase separation phenomena.

Note S3: Crystallization behavior and mechanism of BPCM prepared via RPS, LPS and LTPS

As shown in Figure. S4A and B, for RPS, the SCs of a BPCM have a high crystallinity of 43.1%. This is because the molecular chains, uniformly dispersed in the solution after intense agitation, are rapidly discharged into the crystal lattice during solute precipitation. For LPS, the delay in phase separation provides sufficient time for molecular chains migration, resulting in the microphase separation. It significantly lowers the SC crystallinity to 25.7% while raising the HC crystallinity from 5.5% to 12.4%. Peculiarly, after sufficient cold treatment of the precursor solution, the enhanced chains entanglement promotes chains interaction, inhibits subsequent microphase separation, and prolongs the crystallization time, resulting in a SC crystallinity of 29.7%. Due to their competition with the SC crystallization, HCs undergo a slight reduction of crystallinity to 9.9%.

The crystallite size calculated by eq 6 is shown in Supplementary fig. S4C. To obtain precise values, the SC diffraction peak in (110) plane and the α-HC diffraction peak in (110)/(200) plane are employed to calculate the sizes of HCs and SCs, separately. The SC crystallite sizes are measured as 7.7, 7.0 and 7.7 nm, whereas for HCs these are 6.2, 6.0 and 6.4 nm. In essence, the crystallite size produced by the LTPS technique surpasses that made by LPS; it is comparable with the value prepared by RPS. This underscores that the appropriate cold treatment of the solution not only facilitates the formation of a bi-continuous structure within the metafilm but also supports the growth of crystallites.

In Figure S4D, DSC curves are more appropriate for analyzing the melting crystallization behavior of the samples, with the detailed thermal performance data compiled in Table S2. BPCM consistently displays two melting regions at 160–180 ^{o}C and 200–240 ^{o}C, corresponding to HCs and SCs, respectively. Furthermore, there is no observable cold crystallization at low-temperature stages. HCs exhibit distinct double-peak features, attributed to the melting, recrystallization, melting process during heating[1, 2].

Note S4: HC/SC crystallinity, estimated crystallite sizes and evolutionary mechanism of BPCM with different PLLA and PDLA ratios

In Figure S7, the HC sizes of four metafilms are 6.8, 6.8, 7.7 and 6.9 nm, respectively, while the SC sizes of L7/D1, L3/D1 and L1/D1 are 7.6, 6.4 and 5.7 nm, respectively. Compared to pure PLLA, the HC size of L7/D1 does not change. L3/D1 generates fewer HCs with larger sizes and more SCs with smaller sizes. Of all, the SC size of L1/D1 is the smallest. When the PLLA/PDLA ratio is 1/1, the high and comparable concentration of both enantiomeric chains increases the likelihood of microphase separation, as PLLA and PDLA chains tend to aggregate with their respective counterparts. In contrast, at a 3/1 ratio, the minority PDLA chains are more uniformly dispersed within the PLLA-rich matrix, making phase-separated PDLA domains less likely to form. Even if microphase separation occurs, PDLA chains are more prone to migrate between similar PLLA-rich regions rather than forming isolated PDLA clusters. This mechanism is illustrated in Figure S8.

Supplementary Figures

Figure S1. The photograph and thickness of BPCM prepared by LTPS.

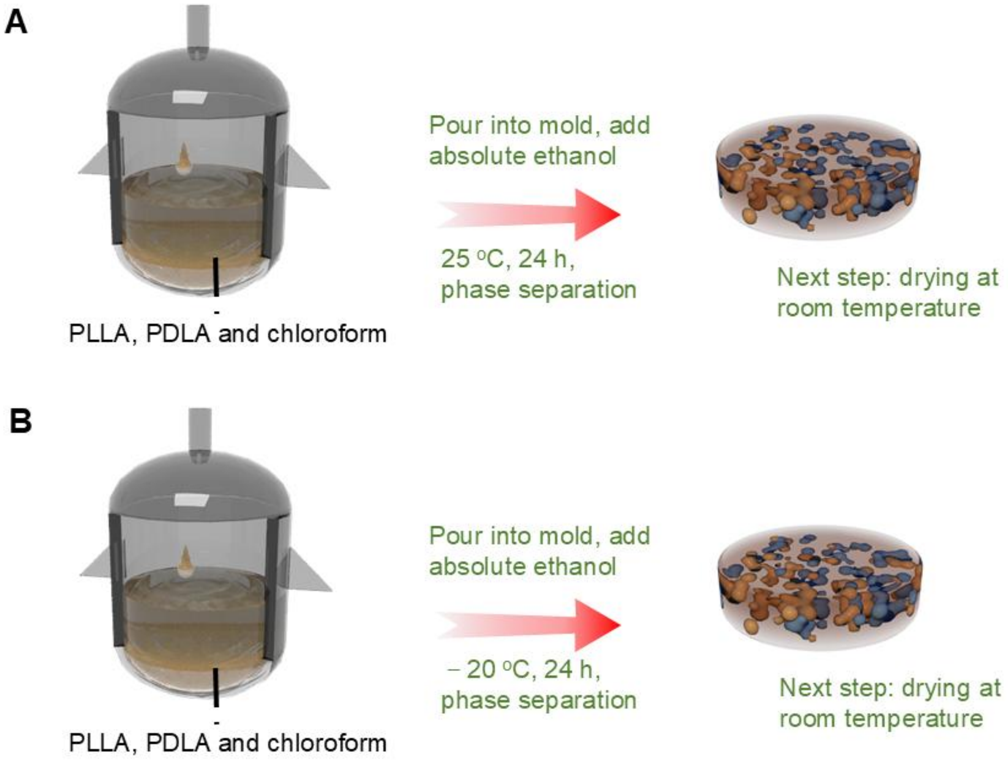

Figure S2. Fabrication of the BPCMs prepared by other methods.

(A) The fabrication of RPS metafilm.

(B) The fabrication of LPS metafilm.

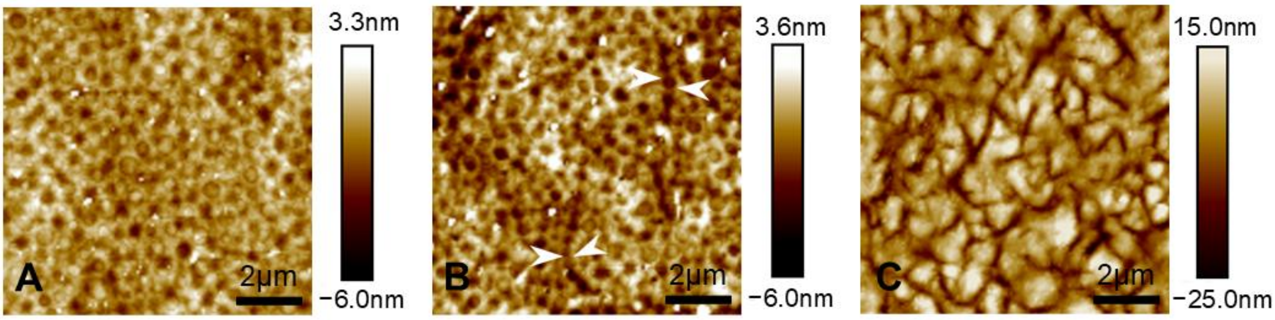

Figure S3. AFM images of PLA films spin-coated from solutions with different cold treatment durations.

(A) Non-cold treated (0 h).

(B) Moderately cold treated (12 h).

(C) Excessively cold treated (24 h).

The scale bars represent 2 μm.

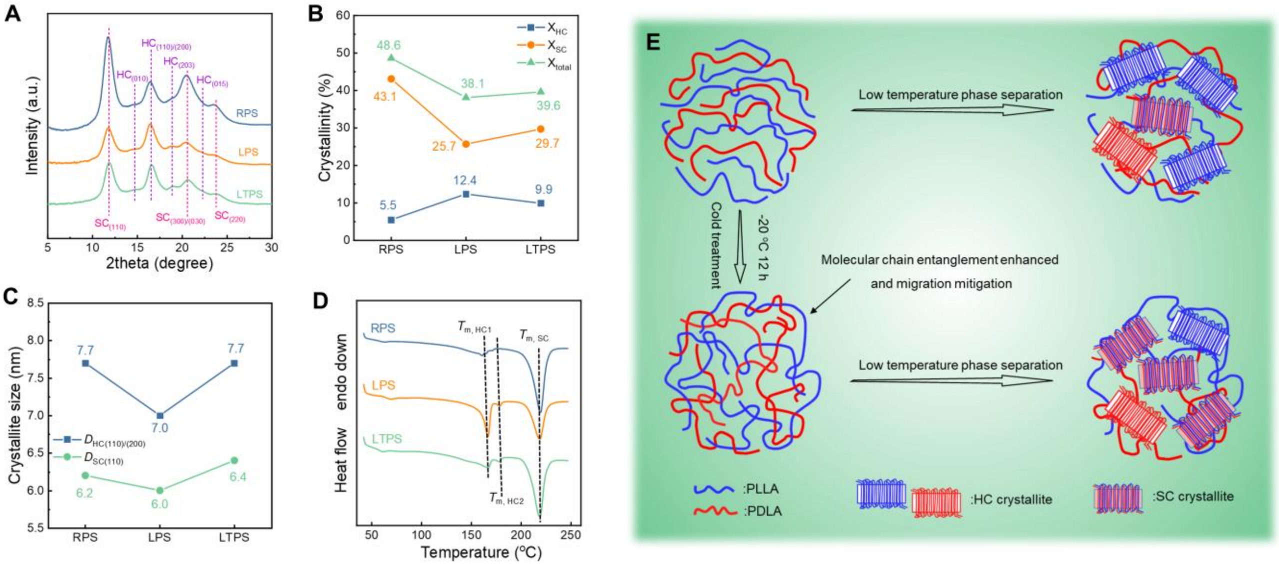

Figure S4. Crystalline structure, thermal behavior, and crystallization mechanism of BPCMs prepared by different methods.

(A) WAXD curves.

(B) HC/SC crystallinity.

(C) Estimated crystallite sizes.

(D) DSC heating curves.

(E) Proposed crystallization mechanism.

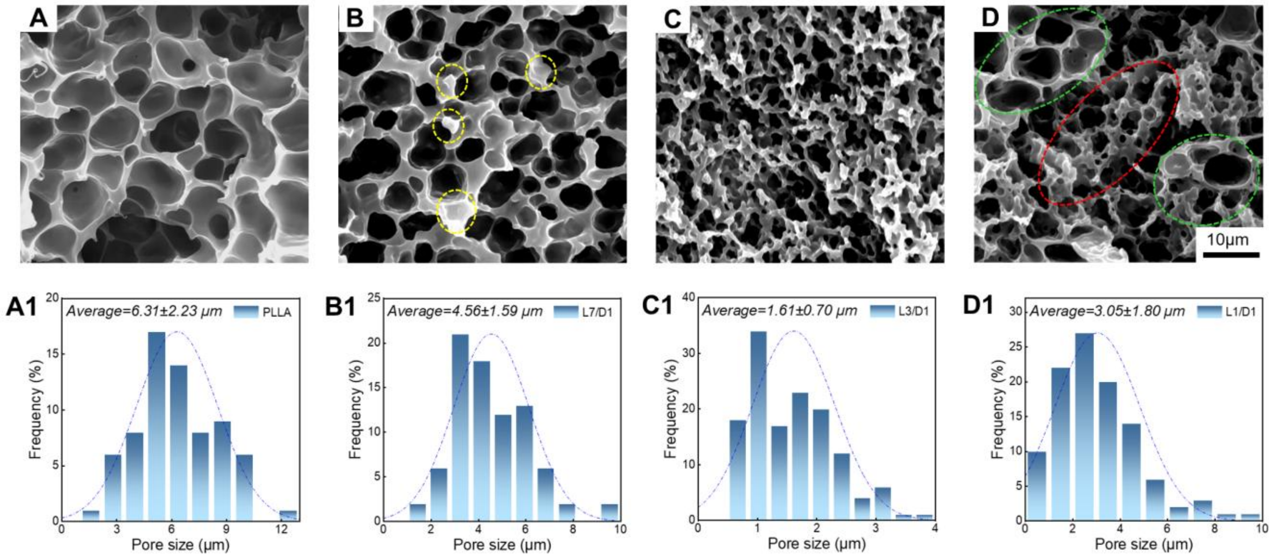

Figure S5. Morphology and pore size analysis of BPCMs with different PLLA/PDLA ratios.

(A–D) SEM images of PLLA, L7/D1, L3/D1, and L1/D1, respectively. The scale bar represents 10 μm, applying to all four SEM images.

(A1–D1) Corresponding pore size distributions.

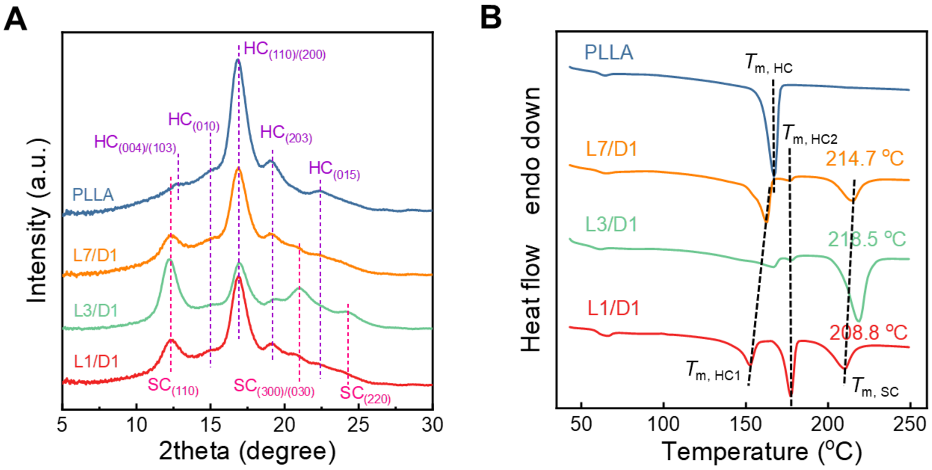

Figure S6. Crystalline structure and thermal behavior of BPCMs with different PLLA/PDLA ratios.

(A) WAXD curves of PLLA, L7/D1, L3/D1, and L1/D1.

(B) DSC heating curves of the corresponding samples.

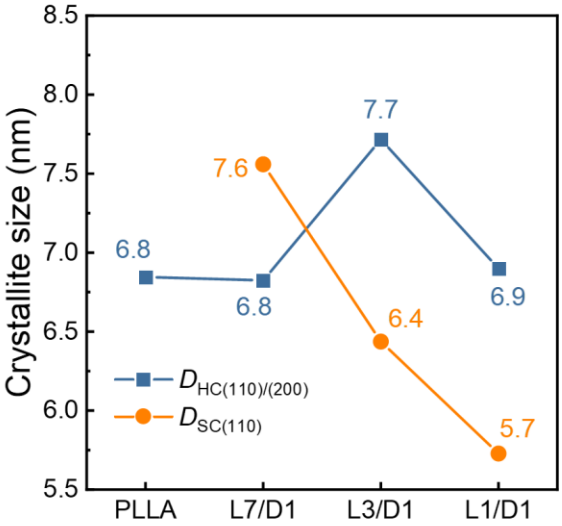

Figure S7. Estimated crystallite sizes of BPCMs with different PLLA/PDLA ratios.

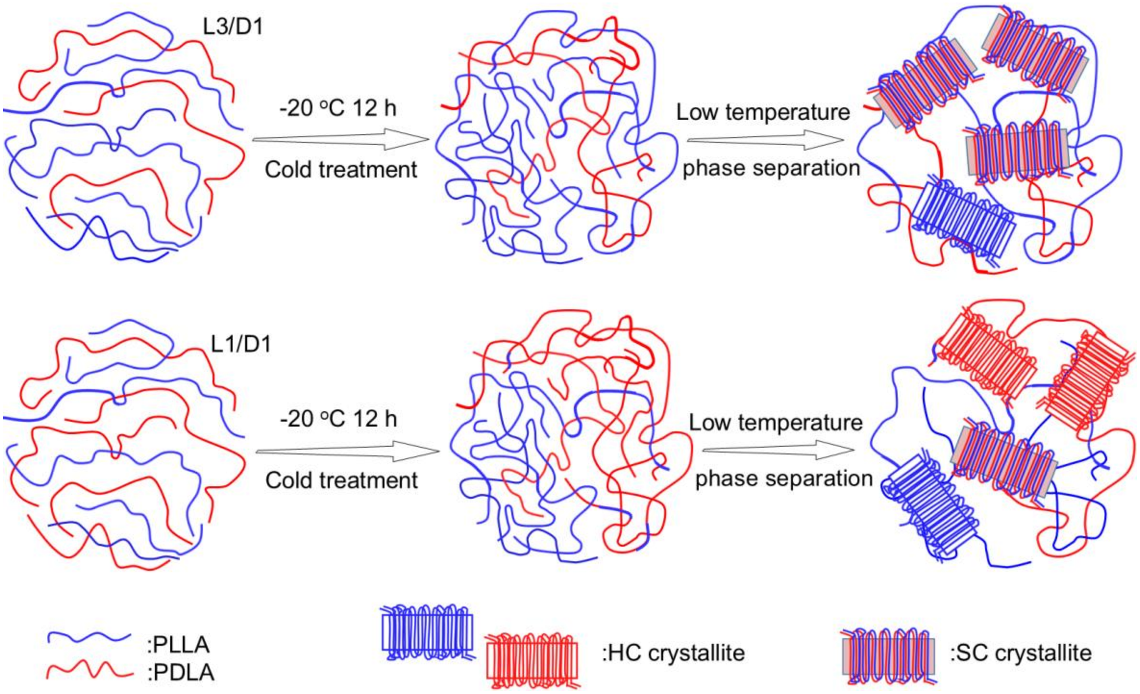

Figure S8. Crystallization mechanism diagrams of L3/D1 and L1/D1 samples prepared LTPS.

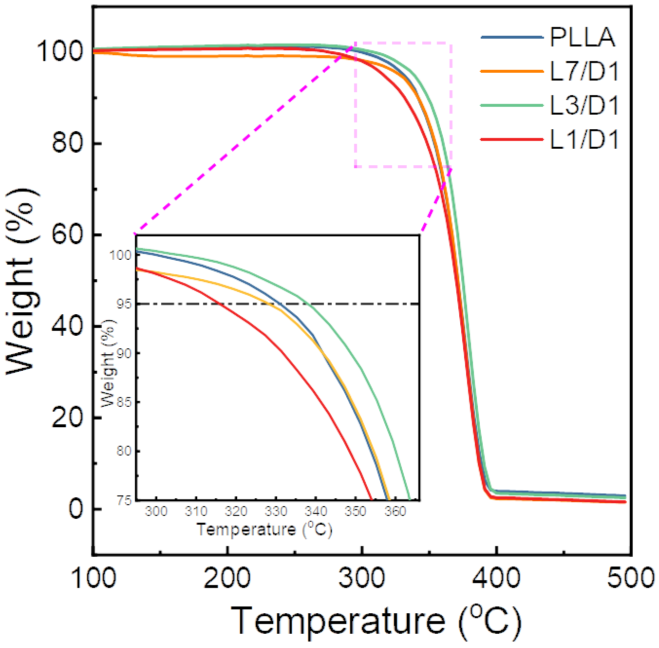

Figure S9. TGA curves of BPCMs with different PLLA/PDLA ratios.

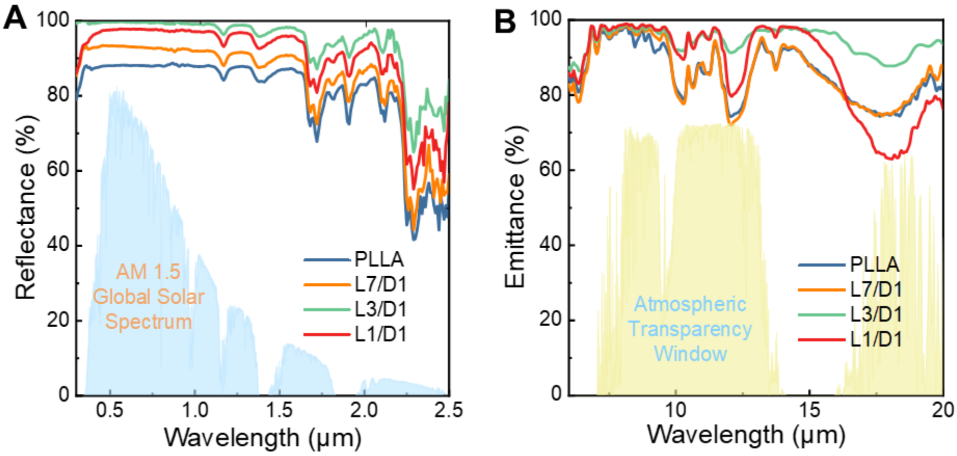

Figure S10. Optical properties of BPCMs with different PLLA/PDLA ratios.

(A) Solar reflectance spectra of PLLA, L7/D1, L3/D1, and L1/D1.

(B) Infrared emittance spectra of the corresponding samples.

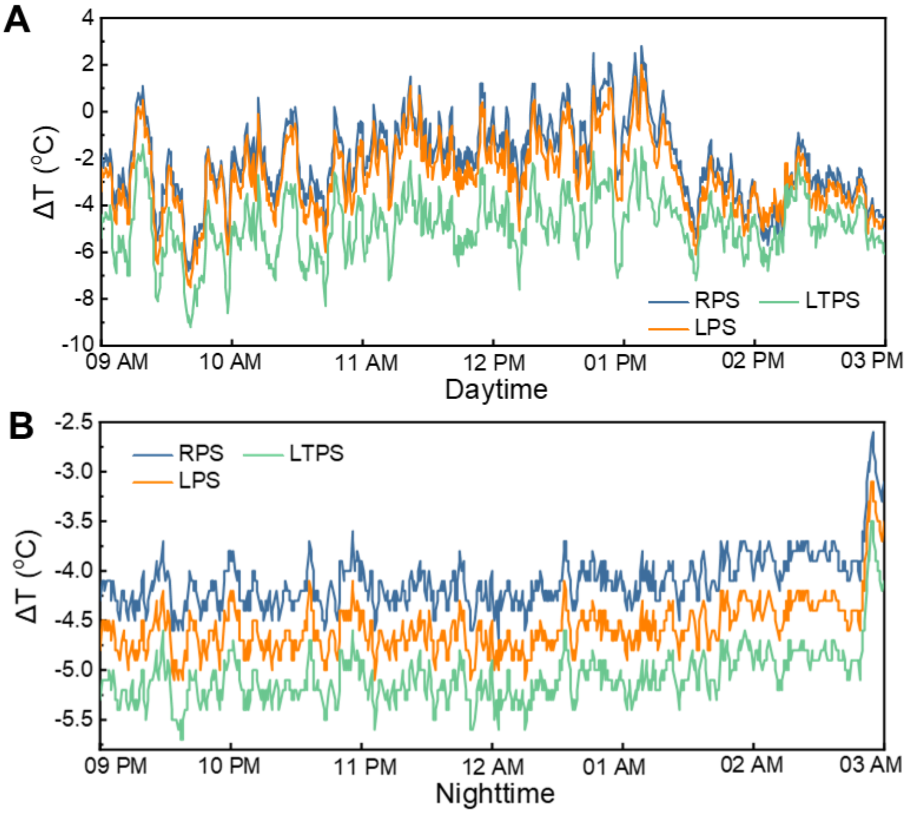

Figure S11. Extracted temperature differences of BPCMs prepared by different methods.

(A) Daytime temperature difference.

(B) Nighttime temperature difference.

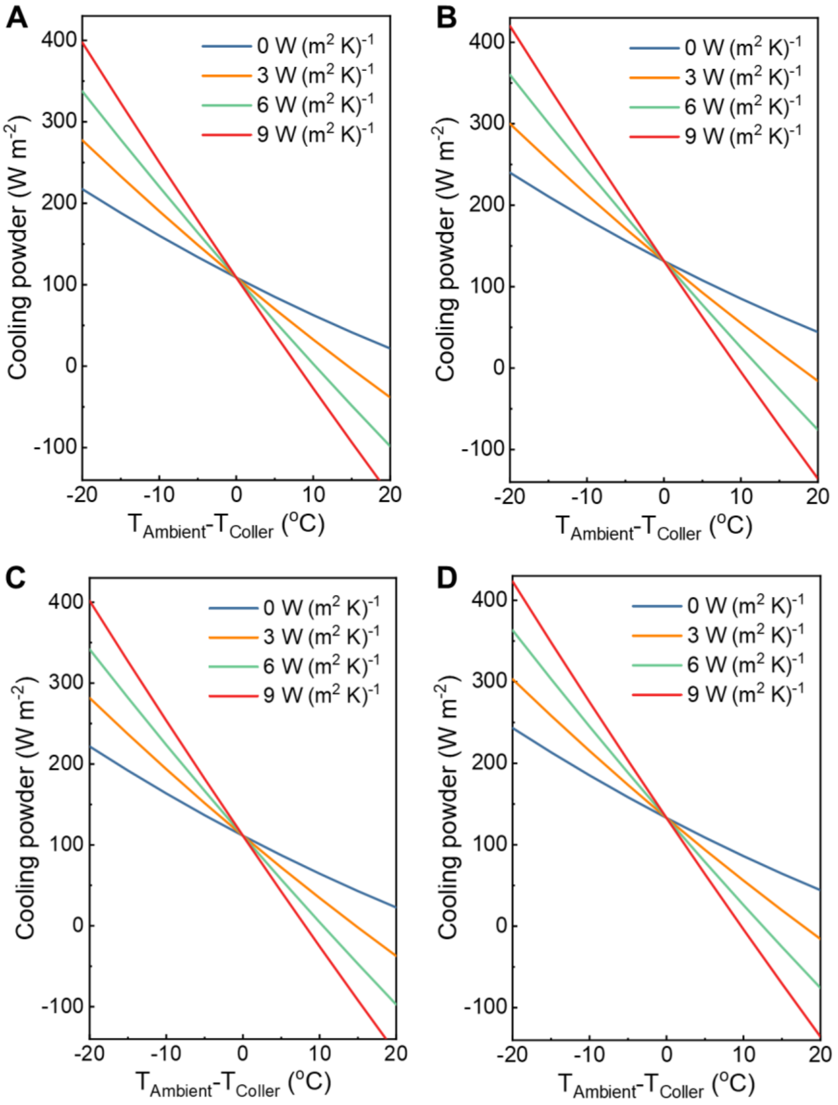

Figure S12. Calculated cooling power of RPS and LPS under different conditions.

(A, B) Cooling power of RPS during daytime and nighttime.

(C, D) Cooling power of LPS during daytime and nighttime.

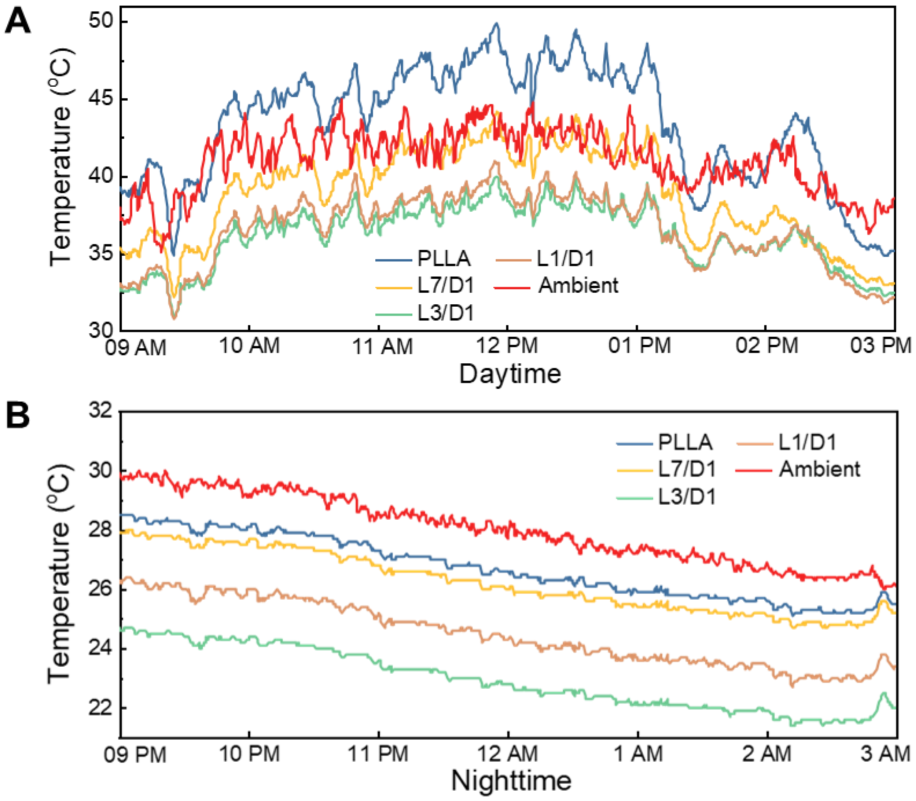

Figure S13. Sub-ambient cooling performance of BPCMs measured in Zhengzhou, China.

(A) Daytime temperature measurement.

(B) Nighttime temperature measurement.

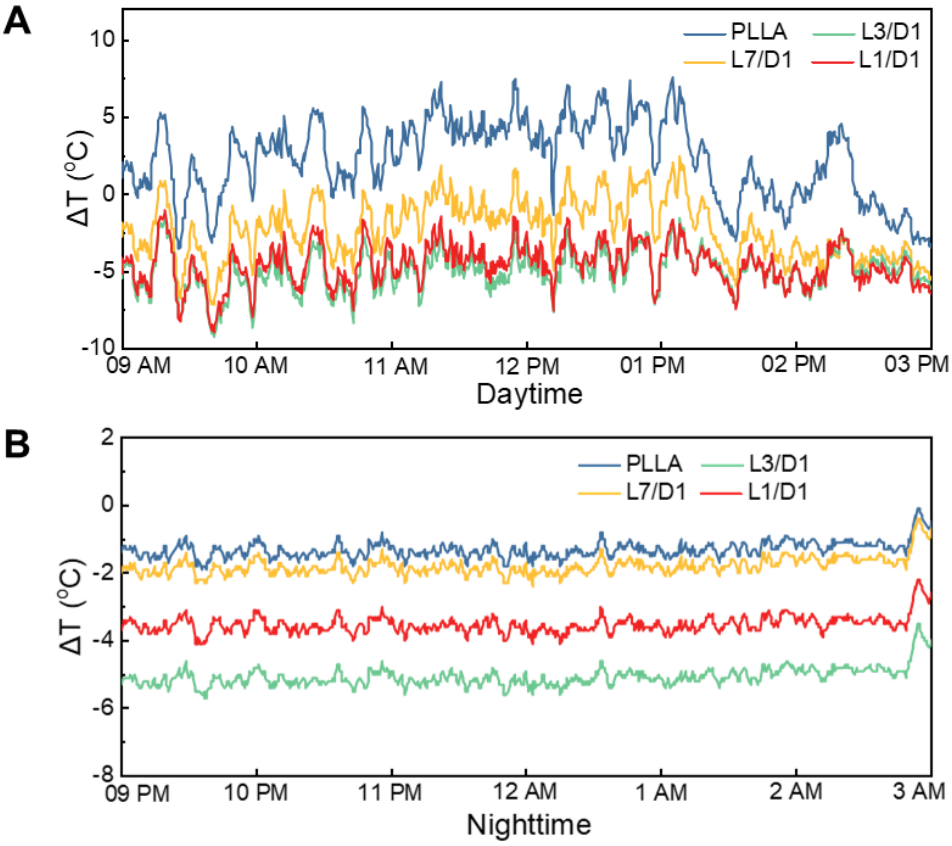

Figure S14. Extracted temperature differences of BPCMs.

(A) Daytime temperature difference.

(B) Nighttime temperature difference.

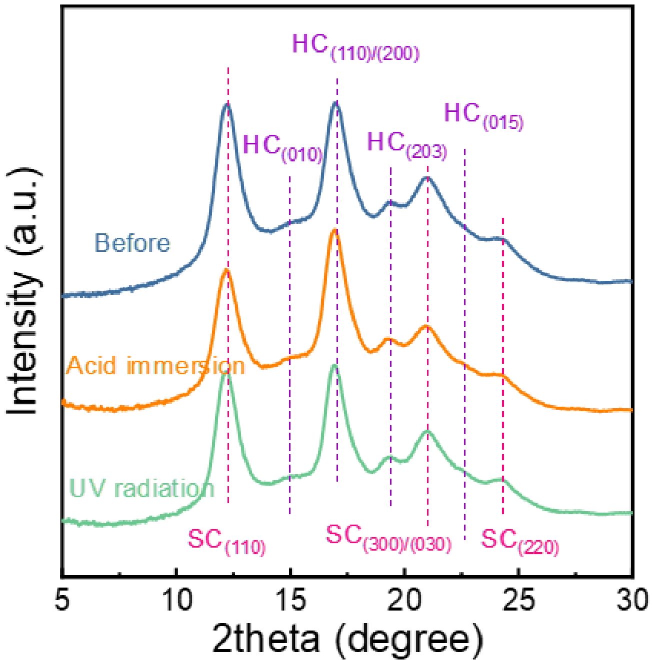

Figure S15. WAXD curves of BPCM before and after exposure to acid immersion and UV radiation.

Supplementary Tables

Table S1. Formulation of BPCMs with different L/D ratios.

	PLLA (g)	PDLA (g)	Chloroform (ml)	Absolute ethanol (ml)
PLLA	0.70	0	10	10
L7/D1	0.61	0.09	10	10
L3/D1	0.53	0.18	10	10
L1/D1	0.35	0.35	10	10

Table S2. Thermal properties of BPCMs prepared by RPS, LPS and LTPS.

	RPS	LPS	LTPS
T_g (°C)	63.7	68.9	63.9
$T_{m,HC1}$ (°C)	162.0	166.3	167.3
$T_{m,HC2}$ (°C)	170.5	178.4	177.9
$T_{m,SC}$ (°C)	219.1	218.4	218.5

Table S3. Thermal properties of BPCMs with different L/D ratios (prepared by LTPS).

	PLLA	L7/D1	L3/D1	L1/D1
T_g (°C)	64.3	65.8	63.9	64.8
$T_{m,HC1}$ (°C)	166.9	162.1	167.3	152.6
$T_{m,HC2}$ (°C)	*	176.4	177.9	176.9
$T_{m,SC}$ (°C)	*	214.7	218.5	208.8

Table S4. Summary of simulated cities, climate zones, and representative seasonal conditions.

City	Country	Köppen–Geiger Climate Zone	Avg. Summer Temp (°C)	Avg. Solar Irradiance (W/m²)	Avg. Relative Humidity (%)	Avg. Diurnal Temp Range (°C)
Sydney	Australia	Cfa (Humid Subtropical)	22–25	680–720	60–70	8–10
Dhabi	UAE	BWh (Hot Desert)	34–37	900–1000	50–60	10–12
Sao Paulo	Brazil	Cfa (Humid Subtropical)	24–26	700–780	70–80	7–9
Lhasa	China	EH (Highland/ Alpine)	18–20	850–950	40–50	13–15
Madrid	Spain	Csa (Hot-summer Mediterranean)	29–32	850–950	40–50	12–14
Nice	France	Csa (Hot-summer Mediterranean)	27–29	800–880	50–60	10–12
Mombasa	Kenya	Af (Tropical Rainforest)	29–31	820–860	75–85	5–7
Singapore	Singapore	Af (Tropical Rainforest)	30–32	780–820	75–85	4–6
Bangkok	Thailand	Aw (Tropical Savanna)	32–34	800–880	65–75	7–9
Phoenix	USA	BWh (Hot Desert)	38–41	950–1050	20–30	15–17

Notes:

Köppen–Geiger classification is based on the updated global climate zone maps by Peel et al.[3]

Avg. Solar Irradiance and Relative Humidity are representative of mid-summer values (June–August in Northern Hemisphere; December–February in Southern Hemisphere).

Data Sources: NASA POWER, NOAA Climate Normals, and World Meteorological Organization (WMO) databases.

Table S5. Performance of BPCM vs. different PRC materials.

Material	Sample	Reflectance	Emissivity	Daytime Cooling	Durability	Degradability	References
Bioplastic	**BPCM**	**98.7 %**	**96.6 %**	**~6.5 °C**	**~ 8 months**	**Yes**	**This work**
Plastic	POM nanotextile	94.6 %	75.7 %	~8.8 °C	~	No	*Ref.* [4]
Plastic	P(VdF-HFP) $_{HP}$ coatings	96.0 %	97.0 %	~6.0 °C	~	No	*Ref.* [5]
Biomass	DNA/gelatin aerogel	100.0 %	90.0 %	~15.1 °C	~	Yes	*Ref.* [6]
Ceramic	Cellular ceramic	99.6 %	96.5 %	~8.8 °C	~ 3 months	No	*Ref.* [7]
Glass	Microporous photonic glass	96.0 %	95.0 %	~4 °C	~ 36 months	No	*Ref.* [8]
PES/Al_2O_3/TiO_2	Organic–inorganic structure	97.0 %	92.0 %	~5 °C	~ 10 months	No	*Ref.* [9]

Notes:

Black front represents PRC materials developed through nanocomposite fabrication or structural design, all of which exhibit excellent optical properties and outdoor cooling performance. However, none have successfully addressed the challenge of balancing degradability, high cooling efficiency, and durability.

PRC: Passive radiation cooling

BPCM: Bioplastic cooling metafilm

POM: Polyoxymethylene

PES: Polyethersulfone

Supplementary References

1. Feng, L., Bian, X., Li, G., and Chen, X. (2021). Thermal properties and structural evolution of poly(l-lactide)/poly(d-lactide) blends. Macromolecules *54*, 10163–10176. https://doi.org/10.1021/acs.macromol.1c01866.

2. Lv, R., Peng, N., Jin, T., Na, B., Wang, J., and Liu, H. (2017). Stereocomplex mesophase and its phase transition in enantiomeric polylactides. Polymer *116*, 324–330. https://doi.org/10.1016/j.polymer.2017.04.004.

3. Peel, M. C., Finlayson, B. L., and McMahon, T. A. (2007). Updated world map of the Köppen-Geiger climate classification. Hydrol. Earth Syst. Sc., *11*, 1633–1644. https://doi.org/10.5194/hess-11-1633-2007.

4. Wu, X., Li, J., Jiang, Q., Zhang, W., Wang, B., Li, R., Zhao, S., Wang, F., Huang, Y., Lyu, P., Zhao, Y., Zhu, J., and Zhang, R. (2023). An all-weather radiative human body cooling textile. Nat. Sustain. *6*, 1446–1454. https://doi.org/10.1038/s41893-023-01200-x.

5. Mandal, J., Fu, Y., Overvig, A. C., Jia, M., Sun, K., Shi, N., Zhou, H., Xiao, X., Yu, N., and Yang, Y. (2018). Hierarchically porous polymer coatings for highly efficient passive daytime radiative cooling. Science *362*, 315-319. https://doi.org/10.1126/science.aat9513.

6. Ma, J., Zeng, F., Lin, X., Wang, Y., Ma, Y., Jia, X., Zhang, J., Liu, B., Wang, Y., and Zhao, H. (2024). A photoluminescent hydrogen-bonded biomass aerogel for sustainable radiative cooling. Science *385*, 68–74. https://doi.org/10.1126/science.adn5694.

7. Lin, K., Chen, S., Zeng, Y., Ho, T. C., Zhu, Y., Wang, X., Liu, F., Huang, B., Chao, C. Y.-H., Wang, Z., and Tso, C. Y. (2023). Hierarchically structured passive radiative cooling ceramic with high solar reflectivity. Science *382*, 691–697. https://doi.org/10.1126/science.adi4725.

8. Zhao, X., Li, T., Xie, H., Liu, H., Wang, L., Qu, Y., Li, S. C., Liu, S., Brozena, A. H., Yu, Z., Srebric, J., and Hu, L. (2023). A solution-processed radiative cooling glass. Science *382*, 684–691. https://doi.org/10.1126/science.adi2224.

9. Li, M., Lin, C., Li, K., Ma, W., Dopphoopha, B., Li, Y., and Huang, B. (2023). A UV-reflective organic-inorganic tandem structure for efficient and durable daytime radiative cooling in harsh climates. Small *19*, e2301159. https://doi.org/10.1002/smll.202301159.